Advances in neutron imaging

Nikolay Kardjilov [1,*], **Ingo Manke** [1], **Robin Woracek** [2], **André Hilger** [3], **John Banhart** [1]

[1] Helmholtz-Zentrum-Berlin, Hahn-Meitner-Platz 1, 14109 Berlin, Germany
[2] European Spallation Source ERIC, Tunavägen 24, 22100 Lund, Sweden
[3] Technische Universität Berlin, Hardenbergstraße 36, 19623 Berlin, Germany

Imaging techniques based on neutron beams are rapidly developing and have become versatile non-destructive analyzing tools in many research fields. Due to their intrinsic properties, neutrons differ strongly from electrons, protons or X-rays in terms of their interaction with matter: they penetrate deeply into most common metallic materials while they have a high sensitivity to light elements such as hydrogen, hydrogenous substances, or lithium. This makes neutrons perfectly suited probes for research on materials that are used for energy storage and conversion, e.g., batteries, hydrogen storage, fuel cells, etc. Moreover, their wave properties can be exploited to perform diffraction, phase-contrast and dark-field imaging experiments. Their magnetic moment allows for resolving magnetic properties in bulk samples. This review will focus on recent applications of neutron imaging techniques in both materials research and fundamental science illustrated by examples selected from different areas.

Introduction

Free neutrons interact differently with matter than electrons, protons or X-rays, and hence imaging techniques based on neutrons are complementary to those based on other types of radiation. Neutrons are chargeless particles but have a magnetic moment [1]. They are absorbed only weakly by many common metals but interact strongly with some light elements [2,3]. Therefore, imaging with neutrons allows for the penetration of thick layers of metals, while providing high sensitivity to light elements.

In recent years, the rapid development of neutron imaging methods by the operators of neutron sources and their users has triggered a tremendous improvement of both spatial and time resolution and furthermore the implementation of techniques that utilize new contrast mechanisms [3–13]. Such developments have now become standard methods for many kinds of investigations. The range of current and potential applications is broad, including general materials research – with a particular emphasis on the area of materials and systems related to the generation and use of renewable energy [14–21] – but also examples from biology [22–24], paleontology [25–29], and cultural heritage [30–33] and specific engineering materials [34]. Imaging with neutrons therefore now belongs to the important non-destructive investigation methods.

One important catalyst for the further improvement of neutron imaging techniques is the rapidly increasing demand for non-destructive and non-invasive in-situ and in-operando investigations of materials and devices that are used for energy supply, such as batteries and fuel cells. Here, the properties and the operation characteristics of the related materials and devices are often closely connected to the distribution and movement of light elements such as lithium and hydrogen. Neutrons have the unique property to be highly sensitive to such light materials, even if these are embedded in a closed metallic environment that strongly absorbs X-rays [2]. The high penetration power of neutrons allows for an investigation of up to 10-cm thick samples. The recently achieved high spatial resolution of a few μm in neutron imaging experiments [35–38] allows one to approach some very interesting phenomena in materials research not accessible by other existing experimental techniques as will be shown in the following sections.

---

* Corresponding author.
E-mail address: Kardjilov, N. (kardjilov@helmholtz-berlin.de).

1369-7021/ https://doi.org/10.1016/j.mattod.2018.03.001

Conventional neutron radiography at continuous sources is based on the transmission of a collimated beam of thermal or cold neutrons through a sample and the recording of the attenuated beam by a position-sensitive detector. The transmitted intensity obeys Lambert–Beer's law stating that for a given neutron energy the ratio of the transmitted and the initial intensity is an exponential function of thickness multiplied by the attenuation coefficient of the sample [39].

The stepwise rotation of a sample in the beam allows for acquiring a set of angular projections that can be used in a second step for tomographic reconstruction. In this way, the entire volume of a sample can be unravelled in 3D by reconstructing the attenuation property for each point of a sample from the collected projections using mathematical algorithms [2,40,41].

In order to provide the highest flux, neutron imaging is often performed with a 'polychromatic or white beam', a term that refers to a broad spectrum of wavelengths (extending over several Å). However, more recently, several imaging techniques have been implemented that utilize well-defined single neutron wavelengths in order to exploit other contrast mechanisms and to overcome limitations related to weak absorption contrast or insufficient spatial resolution encountered in some applications. These limitations have been among the reasons to develop different wavelength-resolved imaging techniques [42] and grating interferometry. The former often utilizes the diffraction contrast [13] that occurs due to Bragg diffraction from atomic lattice planes with d-spacings in the Å range [12,43–45], while the use of grating interferometers [6,46,47] allows for exploiting phase contrast and quantitative dark-field contrast [6,48–50] resulting from sub-μm-sized features in the sample. This allows for investigations of micro and nanostructures in bulk materials. The interaction of the magnetic moment of the neutron with magnetic structures can be used for two- and three-dimensional visualizations of magnetic fields and domain distributions [10,11,51–55].

The relationship between different typical length scales on which various contrast mechanisms operate and some corresponding applications are shown in Fig. 1. Here, each material property (e.g., microstructure, internal defects, corrosion behavior, etc.) or process (e.g., phase transition, water uptake, Li transport etc.) is assigned to a corresponding contrast mechanism that allows to perform a study. The contrasts are obtained by exploiting different types of interactions of neutrons with a sample, and rely either on their particle properties, their wave properties or their magnetic moment and probe materials on different length scales.

The development of high-resolution detector systems currently offers the opportunity to investigate microsystems with spatial resolutions down to or even below 7 μm [35,37]. The combination of such spatial resolutions with innovative imaging methods enables, for example, the direct visualization of magnetic domains or different microstructural properties such as phase distributions, stress and strain fields, textural inhomogeneities, and so on.

Table 1 furthermore categorizes the different contrast mechanisms into experimental techniques, while outlining typical application fields and the general limitations. The table can be used by the reader as guidance through this paper itself, as chapters where corresponding examples are presented are included as well.

While neutron imaging has a long history at reactor-based (steady state) sources, only recently the first two dedicated neutron imaging instruments at pulsed spallation sources became operational, namely IMAT at ISIS (UK) [56] and RADEN at JPARC (Japan) [57,58], and further instruments at the Spallation Neutron Source (VENUS, USA) [59] and the European Spallation Source (ODIN, Sweden) [60], the first long pulse spallation source, are under construction. To fully exploit the timing signature of such pulsed sources, imaging experiments ought to be performed in the time-of-flight (ToF) mode [61–63], in which neutrons spread out and are separated according to their velocities (and hence energies and wavelengths) while they travel from the source to the detector. These developments entail new challenges in detector technology [64,65] and data analysis. Once one can record a complete wavelength spectrum during every neutron pulse produced (typically spallation sources are operated at tens of Hz) fast kinetic studies will become feasible.

Unlike in an earlier review [3] by the authors we focus on recent applications from different areas and provide detailed information on the utilized imaging methodology in this review.

Hydrogen management

Neutrons are very suitable to study hydrogen and hydrogenous materials. In comparison to X-rays, thermal and cold neutrons interact strongly with hydrogen nuclei and small quantities of material containing hydrogen can be visualized even when enclosed by metal or rock.

As an example, the investigation of hydrogen embrittlement and blistering in electrochemically hydrogen-charged technical iron samples by neutron tomography with a spatial resolution of ~25-μm reveals that fine cracks are filled with molecular hydrogen and that cracks are surrounded by a 50-μm wide zone with a high hydrogen concentration, Fig. 2a–d [66,67]. The aim of this study was to reveal how electrochemically charged iron forms hydrogen-induced blisters and cracks. An extended fracture analysis adds information, which is necessary to understand crack initiation and blister evolution.

Hydrogen not only causes degradation of metals, but is also used as an energy carrier and is converted to electric power in mobile devices such as Polymer Electrolyte Membrane (PEM) fuel cells. Safe storage of hydrogen is a key issue in the application of new technologies based on PEM fuel cells in the automotive industry. An innovative solution is the usage of metal hydride composites that store hydrogen chemically and release it upon exposition to higher temperatures. In this way, risks such as explosions of high-pressure hydrogen storage tanks can be avoided. Neutron imaging can be used in such systems to investigate the structural stability and spatial as well as temporal variations of hydrogen concentration in metal hydride composite prototypes during cyclic hydrogenation [21]. Metal hydride composites (MHCs) containing expanded natural graphite exhibit enhanced thermal conductivity and reduced porosity compared to loose metal hydride powders called also "hydride–alumina powders" (HAPs) and are suitable for a reversible, compact and

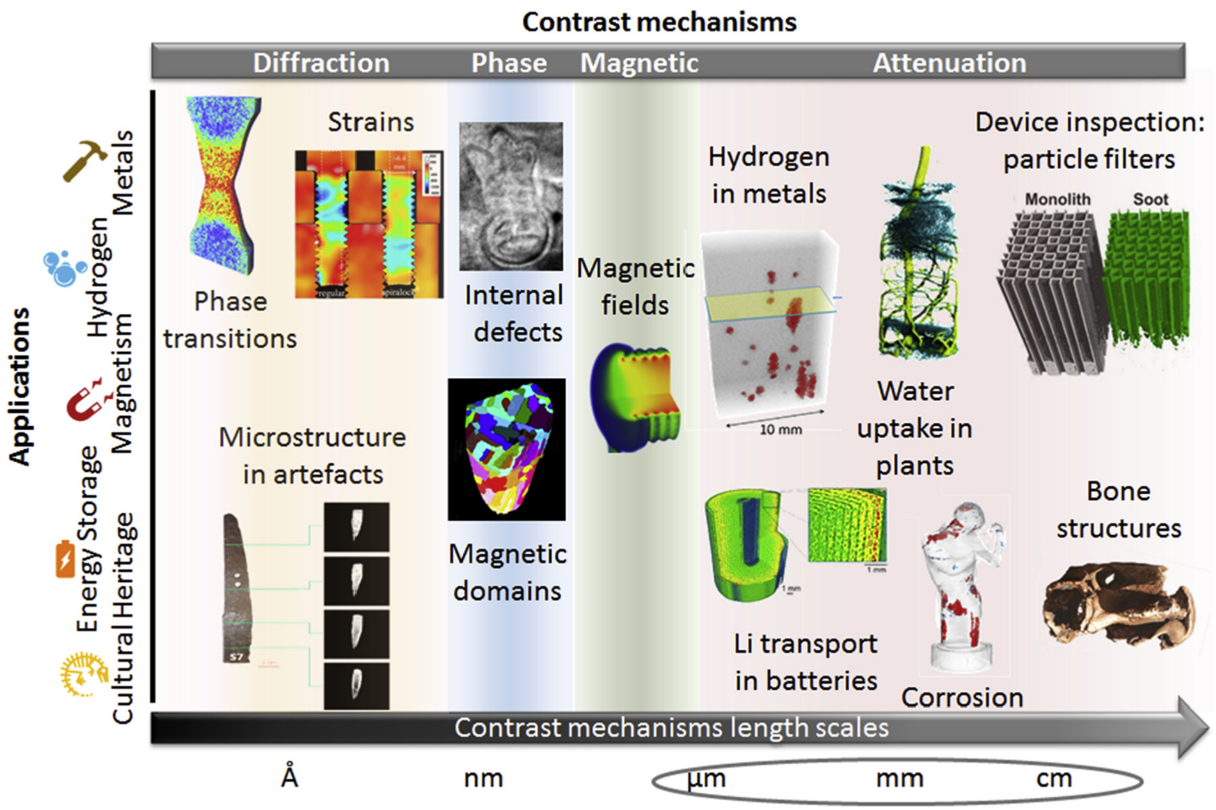

FIGURE 1

Different contrast mechanisms can be used to explore various length scales in materials and to study their properties and related processes. The relation between contrast mechanisms and different application fields is presented. The length scale presented on the lower axis relates to the corresponding contrast mechanism specified on the upper axis. For the attenuation-based image techniques the large length scale was emphasized by grouping the scales from µm to cm.

safe way of hydrogen storage [68,69]. High thermal conductivity is important since it ensures fast and uniform progression of the endothermic (dehydrogenation) and exothermic (hydrogenation) reactions.

In the neutron imaging study presented in Fig. 2e–g, it was found that a loose powder bed (HAP) disintegrated during dehydrogenation, which led to an increased thermal resistance within the hydride bed and to an insufficient heat transfer during subsequent operation. In contrast, MHCs have a larger conducting and the thermal resistance between a MHC and the container wall was reduced since the initial gap closes during the first hydrogenation step and does not reopen after. Further cyclic hydrogenation caused cyclic and almost reversible volume changes of the MHC (so-called "MHC breathing"). Fig. 2f and g demonstrate that the reaction fronts within the MHC and the HAP can be visualized in-operando by neutron radiography. In this study, a commercially available AB_2-type Ti–Mn-based hydrogen-absorbing alloy called Hydralloy $C5_2$ was used, which absorbs hydrogen up to about 1.8 wt.%.

Neutron imaging has been used very successfully to promote the understanding and improvement of polymer electrolyte membrane fuel cells (PEMFCs) [70–72]. Dynamic radiography provides the water distribution in devices operating under realistic conditions [73,74]. Water is the final product of the electrochemical process in such cells. Liquid water generates flow from the catalyst layers toward the gas flow channels through the gas diffusion layer (GDL) under the influence of capillary pressure in a direction opposing oxygen diffusion, Fig. 3a. In order to improve gas transport and reduce water accumulations in the GDL, the wetting properties of the materials used can be selectively tuned [75]. Novel GDL materials with patterned wettability were fabricated by a method based on radiation grafting, i.e., by changing the hydrophobicity by ion radiation, and were investigated by neutron imaging, Fig. 3b.

The quantified water thickness and saturation in a selected region was measured for different applied capillary pressures. The neutron images show that the hydrophilic stripes in the GDL material start to fill with water when increasing the capillary pressure up to 40 mbar, Fig. 3c. For higher pressures, lateral spreading is observed and a saturation level close to 100% is reached, while the stripes broaden to around 400-µm width. Complete saturation of the material and therefore loss of structuring occurs at ~50-mbar pressure. The observed behavior suggests a design for potentially improved water removal from an operating fuel cell: liquid water will flow through predefined hydrophilic regions toward the flow channels (and subsequently leave the cell) while the dry hydrophobic regions are responsible for high gas diffusivity.

A similar improvement of GDL materials can be achieved with an array of small holes (diameter typically tens of µm) in the hydrophobic gas diffusion layers [76–78], Fig. 3d. The role of these holes is to collect water from the surroundings and in this way free

TABLE 1

Summary of the experimental neutron imaging techniques presented in this paper together with the related applications and generalized limitations.

Technique	Applications	Limitations
High-resolution imaging (see chapters 2, 3, 6–9)	Hydrogen embrittlement in metals; Microstructure of metals, geo materials, and bones; Plant's physiology; Lithium distribution in batteries; Water management in fuel cells; Device inspection (corrosion, soot, etc.)	Long exposure times (in the range of minutes per single image); Resolution: 5–30 μm; Small field of view (in the range of several mm^2)
High-speed imaging (see chapters 2, 6)	Water dynamics in plants and fuel cells; Cycling of Li batteries; Cycling of hydrogen storage materials	Exposure times: 1–1000 ms; Moderate spatial resolution (between 0.2 and 0.5 mm)
Wavelength-selective imaging (see chapters 4, 8)	Enhanced element sensitivity; Phase distributions in structural metals and geo materials; Structural phase transitions; Texture and strain fields; Production processes used in objects of cultural heritage interest (swords, armors, etc.)	Long exposure times (in the range of minutes per single image); Moderate spatial resolution (between 0.1 and 1.0 mm)
Grating interferometry (see chapters 5)	Areas of porosity and structure heterogeneity; Magnetic domains in electric steels; Vortex structure in superconductors; Microstructural phase transitions Quantitative particle size analysis in bulk and solutions	Long exposure times (in the range of minutes per set of images); Resolution: 50–200 μm; Sensitivity to vibrations and temperature fluctuations
Polarized neutron imaging (see chapter 5)	Visualization and quantification of weak magnetic fields (~mT) inside and around materials; Visualization of current flow in conductors (skin effect); Optimization of electric devices (motors, etc.); Flux trapping in superconductors; Magnetic phase transitions	Long exposure times (in the range of minutes per single image); Coarse spatial resolution (between 0.5 and 2.0 mm)

the paths through the porous GDL and allow for easier oxygen supply. High-resolution neutron tomography was able to visualize draining of water by holes of 80 μm diameter and to show that the water is distributed in the GDL matrix in the vicinity of the holes, Fig. 3e. Transmission electron microscopy showed that overheating of the GDL material during laser drilling is responsible for the changes of hydrophobicity. The problem was solved by drilling holes mechanically. Eventually, the performance of the fuel cells was improved by up to ~40% [79,80].

In addition to GDL material optimization, different flow field geometries can be used [81–88]. For the example presented in Fig. 3f–h, three basic flow field designs were investigated: a patterned structure, meandering channels, and straight channels [81]. The fuel cells were operated at different conditions while neutron radiographs were taken continuously with repetition rates of 10 s. In this way, the dynamics of water distribution in the flow fields was observed in-operando. For each design, the conditions under which water was removed in the most efficient way were determined.

The data obtained show that the design involving the meandering flow field, Fig. 3g, provides a high stationary power output in combination with an almost constant water content. The meandering flow field exhibits the best capability to remove condensed water. Both the fuel cells containing the patterned structure or the straight channels feature a continuously decreasing output voltage and a low pressure drop. For the straight channels with a higher cross-sectional area in comparison to the other designs and a corresponding low pressure drop, a water agglomeration is visible in the middle of the flow field at low and high current densities, Fig. 3h.

A very special contrast enhancement unique in neutron imaging is it to switch the gas feed from hydrogen to deuterium during operation of the fuel cells. The now produced D_2O has a much lower attenuation than H_2O and allows for the investigation of the velocity of locally different liquid water exchange processes [89,90].

Aside from hydrogen-driven PEM fuel cells, neutron imaging has been widely used for investigation of gas distribution in direct methanol fuel cells [91–94] and recently to study acid distribution in high temperature PEMFCs [95–97]. Recent successful applications using wavelength resolved neutron imaging (see chapter 4) have also included the phase transition in Solid Oxide Fuel Cells (SOFC's) [98,99].

Batteries

Neutrons are ideally suited to investigate devices for chemical energy storage due to their high sensitivity to charge carriers such as Li ions and to the hydrogen-containing electrolytes involved [15,100–107]. Li-ion batteries are a rewarding object because the migration of Li-ions can be visualized [100,108], which helps to identify areas of reduced activity that are responsible for capacity fading. During charge and discharge, a dynamic measurement of the change in lithium ion concentration can be performed by measuring the change in neutron transmission.

The study presented in Fig. 4a–c was performed in a pouch cell consisting of alternating double-sided current collectors: $LiFePO_4$ on aluminum for the positive electrode and carbon on copper for the negative electrode [109]. The multi-layered sheets of electrode material were folded to produce a ten-layer pouch cell. This planar pouch cell has a unique advantage over cylindrical

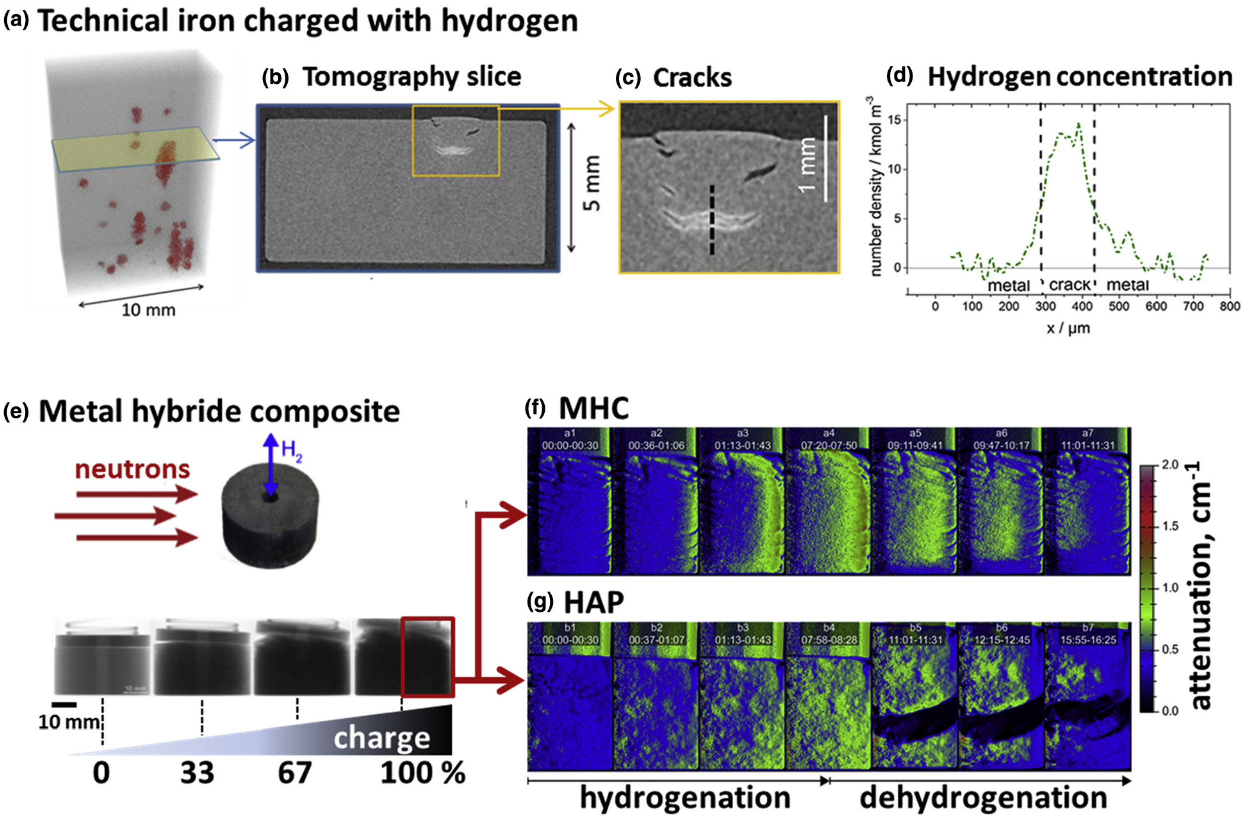

FIGURE 2

Hydrogen in metals: (a) Example of high-resolution tomography of technical iron (ARMCO iron) that was electrochemically charged with hydrogen [66,67]. The highly attenuating hydrogen is marked in red. (b) Embrittlement and blistering effects are well visible in the tomographic reconstruction. (c) Some of the cracks are filled with hydrogen (bright cracks) while the cracks close to the surface are free of hydrogen (dark cracks). Hydrogen diffusion in the area around the cracks is observed too. (d) Hydrogen concentration profile along the dashed line in the tomographic image (c). (e) Metal hydride storage materials were investigated by neutron imaging during cyclic hydrogenation and dehydrogenation. A general view of the hydrogenation process in a metal hydride composite (MHC) is shown in 4 radiographs. The field of view selected for neutron radioscopy is marked by a red rectangle; (f and g) spatio-temporal hydrogen concentrations in a MHC of 40-mm diameter compared to loose hydride–alumina powders (HAPs) both contained in a cylindrical container were studied to evaluate their structural stability [68,69].

designs in that the anode and cathode layers are easy to distinguish in radiographic neutron images after aligning the battery using a stepper motor so that the optical axis is parallel to the electrode sheets. In this orientation, Li ion migration between the anode and cathode electrodes can be observed during charge and discharge.

The optical density (i.e., the change in local attenuation) defined as the negative logarithm of the ratio of two radiographs taken at different States of Charge (SOC) is proportional to the lithium concentration. The reference state is taken to be almost fully charged (T4 = 99%), so that lithium accumulation (positive values of optical density) occurs in the cathode layer when the battery is discharged relative to the reference. The negative electrode loses lithium and, therefore, the optical density decreases. Fig. 4b shows the change in optical density for the first two layers in the region marked in Fig. 4a.

The decrease in optical density in the anode and an analogous increase in the cathode during discharge is shown at 50% SOC (T5 = half charged) and 0% SOC (T6 = discharged) in Fig. 4b. The measured peak displacements in the corresponding transmission profiles, Fig. 4c, can be related to the shrinkage of the active material upon discharge consistent with the assumption of expansion due to Li intercalation. The average displacement corresponds to a 3% change of thickness if attributed solely to the anode active material, which is within the range of 0–7% predicted by Fuller et al. [110].

In another example, the high sensitivity of neutron imaging to Li was again exploited to study another type of battery: the Li-air system [111]. The spatial variation of discharge products across the bulk of a Li-air electrode was visualized by neutron tomography, Fig. 4d. 3D tomographic reconstruction of the electrode shows a non-uniform distribution of lithium across the thickness of the electrode, while the lithium concentration is observed to be higher near the edges of the Li-air electrode and relatively uniform in the center of the electrode, Fig. 4e.

A 3D transport model including reaction kinetics and mass transport across the air cathode thickness was applied to understand the results obtained and showed that the origin of such non-uniform product distribution is related to the polarization factors due to the kinetic and diffusion barriers that could lead to a discharge product gradient, Fig. 4f. The result obtained provides essential insights into the discharge mechanism in thick air cathodes that could lead to the design of air cathodes adapted to Li-air chemistry [111].

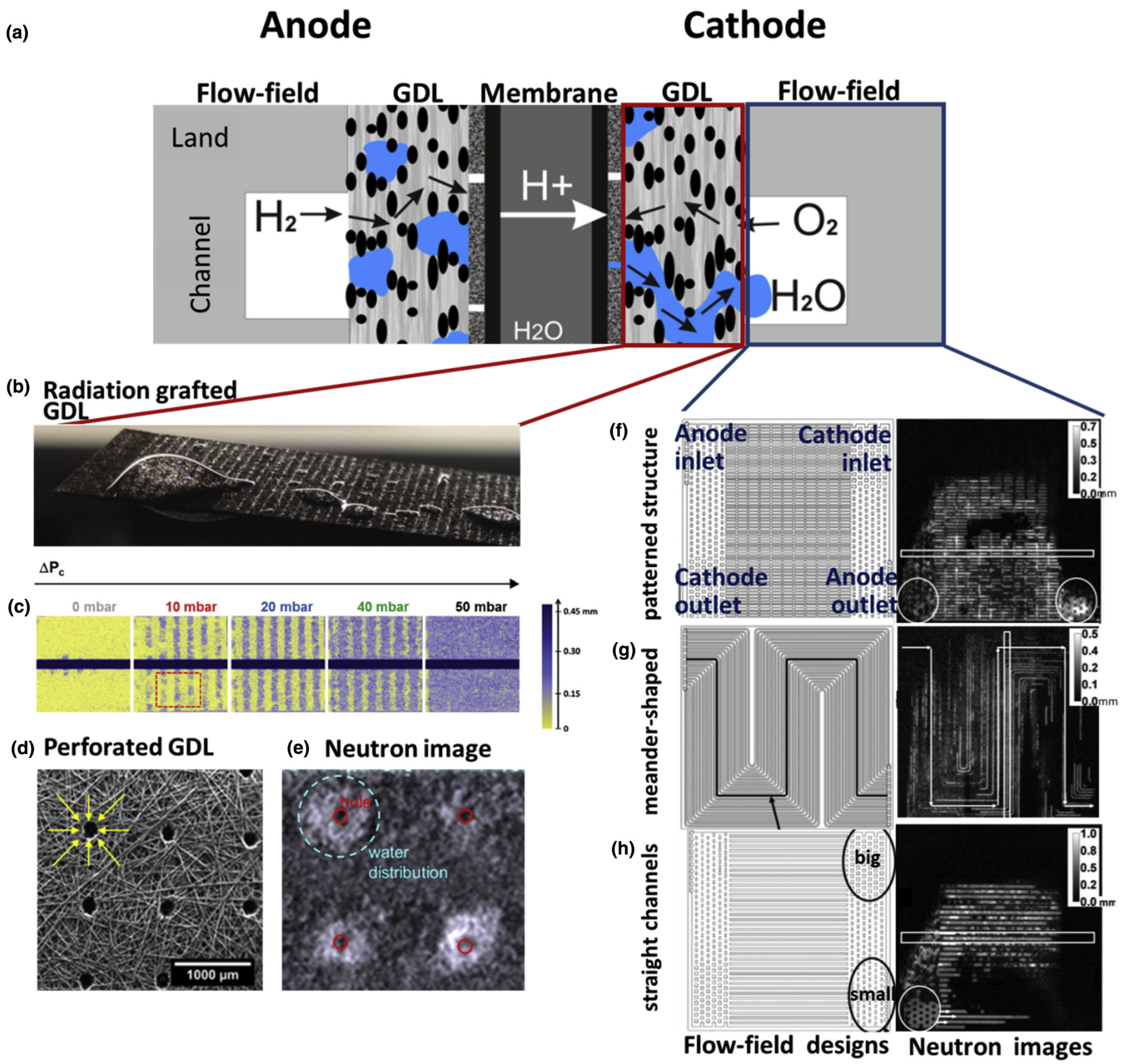

FIGURE 3

Optimization of Polymer Electrolyte Membrane Fuel Cell (PEMFC): (a) Scheme of PEMFC. (b) Photograph of a modified Toray GDL with a periodic pattern of 100-μm wide hydrophilic areas and 500-μm wide hydrophobic areas after immersion in water. (c) Different capillary pressures were applied to the modified GDL (Toray 30% Fluorinated ethylene propylene (FEP) 500–950 μm with N-vinylformamide (NVF)) and the water distribution was measured by neutron radiography. The radiographs show water locations within the GDL with increasing capillary pressure: 0 mbar, 10 mbar, 20 mbar, 40 mbar, and 50 mbar [75]. (d) Proposed new GDL structure with holes that influence water drainage. (e) Neutron tomographic slice through the GDL showing the distribution of water (white areas). (f–h) Comparison of three different flow field designs in a PEFC. Left column: Computer-aided design (CAD) sheets of the cathode flow fields investigated, gas flow directions and characteristic channel lengths are given. Right column: Neutron radiographs of the investigated flow field designs (from top to bottom: patterned, meandering flow field, straight channels) with calculated water thicknesses given mm [81].

Lithiation and delithiation of individual Si anode particles were recently studied by Sun et al. [101]. Another key issue is the gas evolution caused by electrolyte decomposition especially during first activation of Li batteries [102,108,112–114]. Other neutron imaging studies were focused on sodium batteries [115,116], alkaline batteries [15,117], various other lithium battery types [103,104,106,109,118–123], and on transport of ions in carbon [100,119,124]. Wavelength-resolved studies have the potential to monitor the status of Li intercalation through local analyses of the transmission spectra [125].

Metallic materials

The neutron can be regarded not only as a particle but also as a propagating wave [8]. The wavelength for low energetic (cold) neutrons ranges from 2 Å to 6 Å. For such neutrons, Bragg scattering from atomic lattice planes that have distances d_{hkl} of sets of planes of orientation *hkl* comparable to the neutron wavelength occurs. Neutron diffractometers typically probe the diffraction angle (angular dispersive measurements) and/or the wavelength (wavelength dispersive measurements, where the detector is positioned at a given fixed angle) to determine

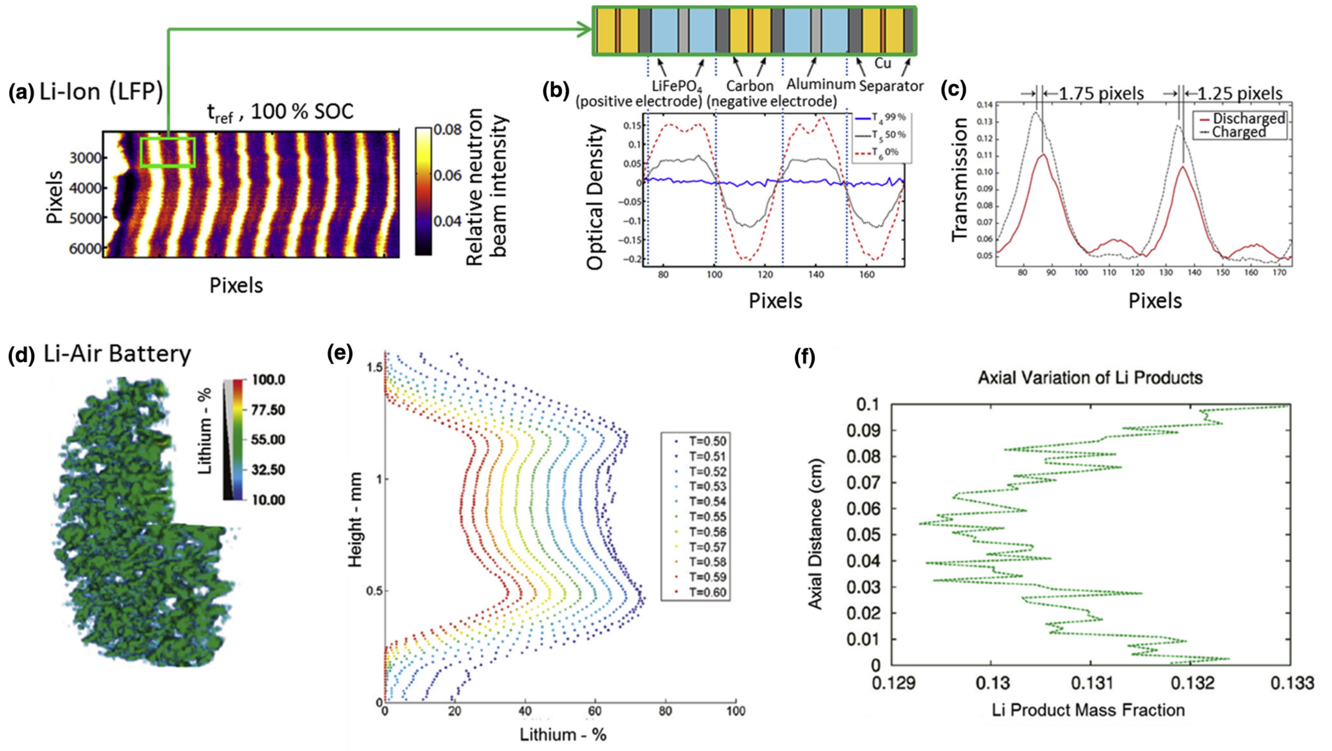

FIGURE 4

Investigation of Li-based batteries: (a) Neutron radiograph of a Lithium Iron Phosphate (LFP) pouch cell, (b) charge and discharge profiles of the optical density (proportional to the lithium concentration) corresponding to different States of Charge (SOC). (c) Transmission profiles showing peak displacements for charged and discharged states. The total thickness of each unit battery is 260 μm, which agrees well with the average peak spacing of 53 pixels or 263 μm. The depth of the pouch cell along the optical axis is $d = 2$ cm. The capacity of the pouch cell is approximately 120 mAh [109]. (d) Reconstructed 3D tomography image of Li-air cathode after discharge for 23,000 s. (e) Calculated line profile showing the relative Li volume fraction (in %) in Li-air cathodes. The line profiles are calculated at different Li concentration thresholds to be able to quantify uncertainty. (f) Li product profiles after 23000 s of discharge as obtained by modeling [111].

the structure of crystalline solids (single crystals, powders, polycrystalline materials). Neutron imaging measurements in transmission geometry are not angular dispersive and probe just the non-diffracted intensity [13,126,127]. For single crystals, one observes characteristic dips in the transmission spectrum while for randomly orientated polycrystalline materials, a sawtooth pattern is observed. The positions of these so-called Bragg edges provide a direct measure of d_{hkl} and therefore carry information on phase [12,128–133] and strain [44,128,129,134–142], while the heights of the specific Bragg edges yield a direct measure of the number of crystallites that have their respective planes oriented normal to the incoming beam and therefore carry information on texture [44,143–149]. Using a position-sensitive detector, these spectra can be displayed in every pixel and hence the method is often termed "Bragg edge imaging", while 'diffraction contrast imaging' is a more versatile term that can also be applied to investigations of single crystal and textured materials.

In order to utilize diffraction contrast in an imaging experiment, wavelength-resolved measurements are needed that can be realized using a tuneable neutron monochromator [42,43] or by wavelength–dispersive time-of-flight measurements [62,63].

A recent study showcased the use of this technique by separating and quantifying two different crystallographic phases in stainless steel [12,132,133]. Metastable stainless steel (ASTM standard 304L) samples were subjected to certain plastic tensile and torsional strains, causing transformation induced plasticity (TRIP), i.e., a martensitic phase transformation in which fcc austenite transforms to martensite (bcc and hcp structures). An example from this study is shown in Fig. 5a–c for two samples subjected to different load types. Tomographic scans were performed by recording 180 projections over a 360° range at two energies, before ($\lambda_1 = 4.1$ Å) and after ($\lambda_2 = 4.3$ Å) the fcc (1 1 1) Bragg edge of the austenitic phase. The most pronounced Bragg edge (or 'Bragg cut-off') occurs at slightly different wavelengths for the two phases, resulting in attenuation differences in the data taken at 4.1 Å. The filtered back-projection algorithm for parallel beam reconstruction was used to individually reconstruct the tomographic data sets.

By normalizing the reconstructed data taken at 4.1 Å by the data taken at 4.3 Å, a ratio of the Bragg edge height is obtained, which can be used for a quantification of the phase fractions. Line profiles as presented in Fig. 5c represent the phase distribution through the reconstructed tomographic data. Neutron diffraction using a $2 \times 2 \times 2$ mm^3 gauge volume was used at selected locations to verify the results derived from imaging data. The values obtained from the images show a good agreement both with diffraction results and simulated data. Diffraction contrast imaging with monoenergetic neutrons can therefore be used as a visualization and quantification tool to study phase transition effects in steels and other metals.

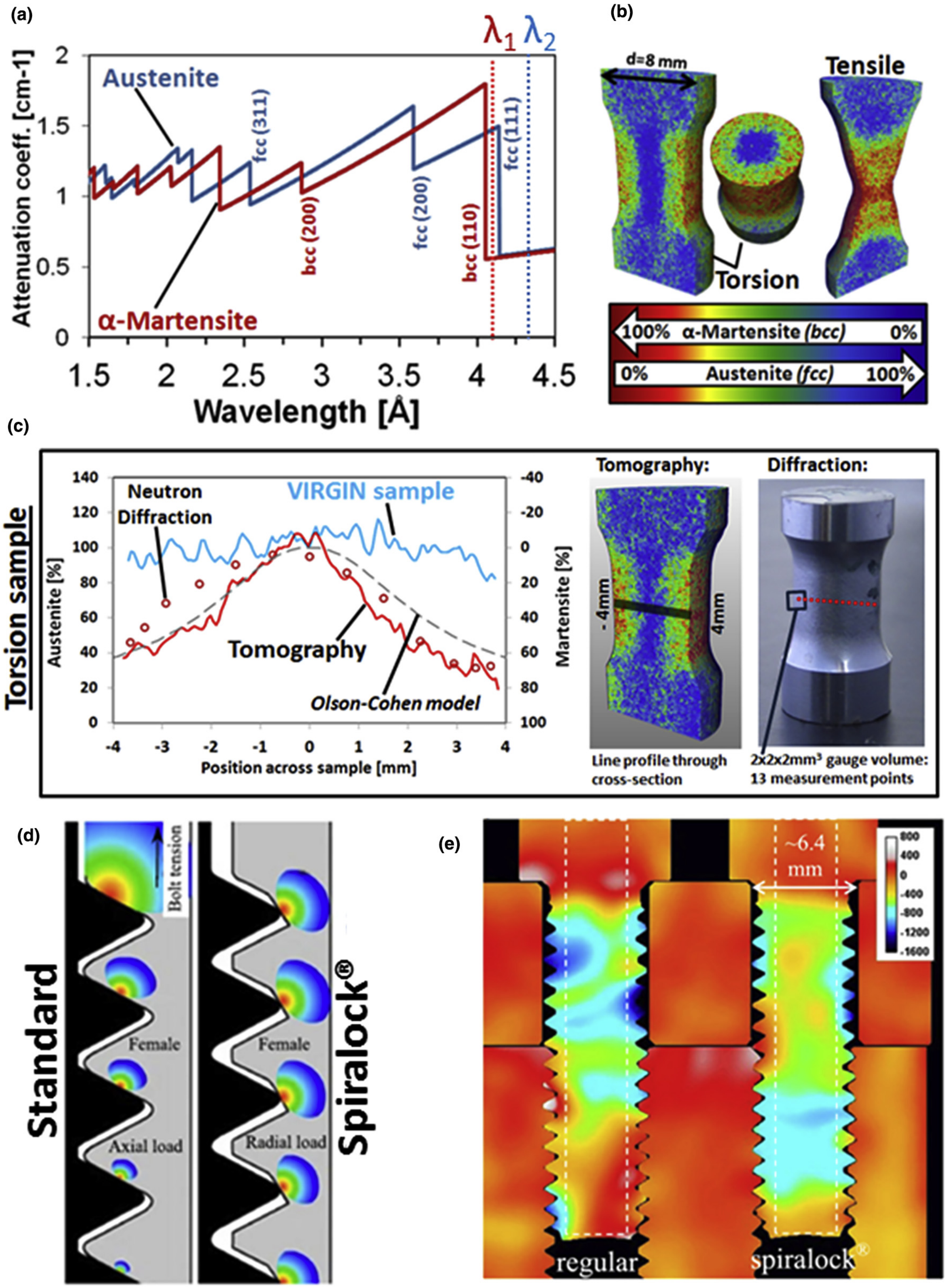

FIGURE 5

Examples of wavelength-selective imaging and Bragg edge analysis. (a) Theoretical attenuation coefficients of austenite and α-martensite. (b) 3D reconstructed phase fractions inside a samples subjected to tensile and torsional loading. Large plastic deformation has led to the formation of martensite. (c) Line profiles along and across the reconstructed data show the phase fractions. Neutron diffraction-based results are included to refer to a standardized characterization method, and the theoretical α-martensite phase evolution is predicted for the torsion sample using the Olson–Cohen model. Results for an undeformed sample (virgin state) are included for matters of comparison [12,132]. (d and e) Another study visualizes the strain variation in an assembly consisting of two stainless steel (fcc) plates (top with through holes and bottom with female threads) and hardened steel (bcc) screws. The left connection uses a standard thread, where the stress is known to be carried non-uniformly by the thread increasing the probability of shear, and the right connection uses a Spiralock® thread that is designed to distribute the load radially. The measured strain maps can be used for the comparison of the loads in the assemblies with respect to vibrational stability of the two thread systems [150].

Moreover, as mentioned above, applied and residual strain can be deduced from the Bragg edge position. An example is depicted in Fig. 5d and e for a comparison of the strain distributions between an assembly relying on a standard thread and a Spiralock© [150]. The strain information in such measurements that are purely based on neutron transmission represents the average strain component along the incident beam direction through the sample thickness. Thus, it remains a non-trivial task to investigate complex strain fields (where the principal strain direction varies along the beam path) and components where the strain magnitude varies through the sample thickness, and usually requires knowledge of additional boundary conditions obtained by modeling or in experiments. Most importantly, however, the method allows for (non-destructive) bulk investigations and can reveal heterogeneities that may remain undetected if only diffraction is used, while other features visible in the tomography data (such as cracks, porosities, etc.) can be visualized simultaneously.

It is expected that neutron imaging will play a vital role for the characterization of parts that are manufactured by Metal Additive Manufacturing (AM), a.k.a. 3D printing, that offers the possibility to produce complex parts without the design constraints of traditional manufacturing routes. While AM was initially seen as tool for rapid prototyping, it has now expanded to the manufacture of parts for various industries [151–153]. The fast emerging possibilities to use AM components for a wide array of applications exposes these at the same time to many different structural and mechanical requirements. Neutron imaging is expected to be capable of providing invaluable information, e.g., about local variations of the microstructure, as can be seen from first studies [154–157].

Energy-selective imaging can be extended to higher neutron energies where the presence of neutron resonances in the epithermal range of energies (from tens to hundreds of eV) can be utilized to map elemental or isotope distributions within samples. It is possible to map the bulk microstructure and elemental composition within materials inaccessible to conventional non-destructive testing techniques. In the example presented, neutron resonance spectroscopy is applied to two single-crystals and two polycrystalline natural gold samples from Venezuela [158]. The experimental setup utilizes a time-of-flight (ToF) arrangement with a single fast neutron counting detector installed at a pulsed neutron beamline. The detector is triggered by the spallation pulses providing both position (X, Y) and time-of-flight (T) for every detected neutron. Multiple neutron pulses were utilized in the ToF mode, therefore collecting several thousand time-resolved images, with each image corresponding to a specific energy obtained from the graph shown in Fig. 6.

A quantitative analysis of the elemental compositions of the samples is performed by fitting the calculated transmission (assuming natural isotopic ratios for each element) to measured spectra, with the sample thickness and elemental concentration serving as fitted parameters. In addition, the spatial distribution of Au and Pd within the samples can also be reconstructed from the same experimental data as demonstrated in Fig. 6. A gold-specific transmission image can be obtained by dividing the transmission image in Fig. 6d (taken at the resonance energies of gold) by the image in Fig. 6e, obtained in a region of the spectrum where no resonances are present as shown in Fig. 6f. A similar normalization, this time using Pd resonance energies, produces an image of the Pd distribution in the samples as shown in Fig. 6g, indicating that the bulk distribution of palladium in the samples is not uniform.

The ability of neutrons to pass through heavy elements such as lead, gold and silver as shown above is used for the visualization of objects opaque for X-rays. Another example of this can also be seen in Fig. 13c–f, where a sculpture made of lead was investigated by neutron tomography allowing one to assess its present state of conservation.

Magnetic materials

Neutrons possess a magnetic moment which allows for detecting and quantifying magnetic properties in bulk samples. Using a beam of high spatial coherence, for example, walls between magnetic domains (Bloch walls) can be visualized by means of a grating interferometer in which a source grating with stripes of a few hundred μm width produces an array of multiple line sources that define a spatially coherent beam illuminating a phase grating [5,11,159–163]. At a certain distance behind the phase grating, an interferential pattern can be observed. The structure of this pattern, which is beyond the spatial resolution of the imaging detectors, can be resolved by scanning an analyzer grating through the beam in a transverse direction, Fig. 7a. The presence of a sample distorts the interference pattern locally, as shown in Fig. 7b. Detection and analysis of the pattern yields information about phase effects, small angle scattering and attenuation introduced by the sample. These three signals can be extracted and analyzed independently and provide a unique suite of complementary information about the sample material [164]. By rotating the sample and collecting projections at different angles tomographic 3D reconstruction of the three signals is possible [6].

When magnetic samples are used in this setup, neutrons are scattered by the volume between two domains and in return cause a reduced amplitude of the interferential pattern as shown in Fig. 7b. This change in the amplitude can be detected for each pixel and a corresponding amplitude map can be obtained. This is known as a dark-field image [46]. An example for the application of this method is an investigation of the magnetic properties of high-permeability steel laminates (HPSLs) as a function of the stress induced by the insulating coating layer [51,52]. Such HPSLs are stacked in the core of transformers. Individual plates are covered by an insulating coating in order to reduce eddy-current losses. In addition, the coating also induces intergranular tensile stresses that preserve the alignment of the magnetic domains. Without this stress the structure of the domains changes and their alignment is lost.

In order to analyze the influence of the coating on the volume and supplementary surface magnetic domain structures, grating interferometry can be used as shown in Fig. 7c, d. Dark-field imaging resolves the basic domain walls and shows the alignment of the domains in the coated sample. To visualize the stress effect of the coating on bulk domain formation, the coating of the HPSL sample was removed and external tensile stress was applied stepwise up to a level of 20 MPa. The domain

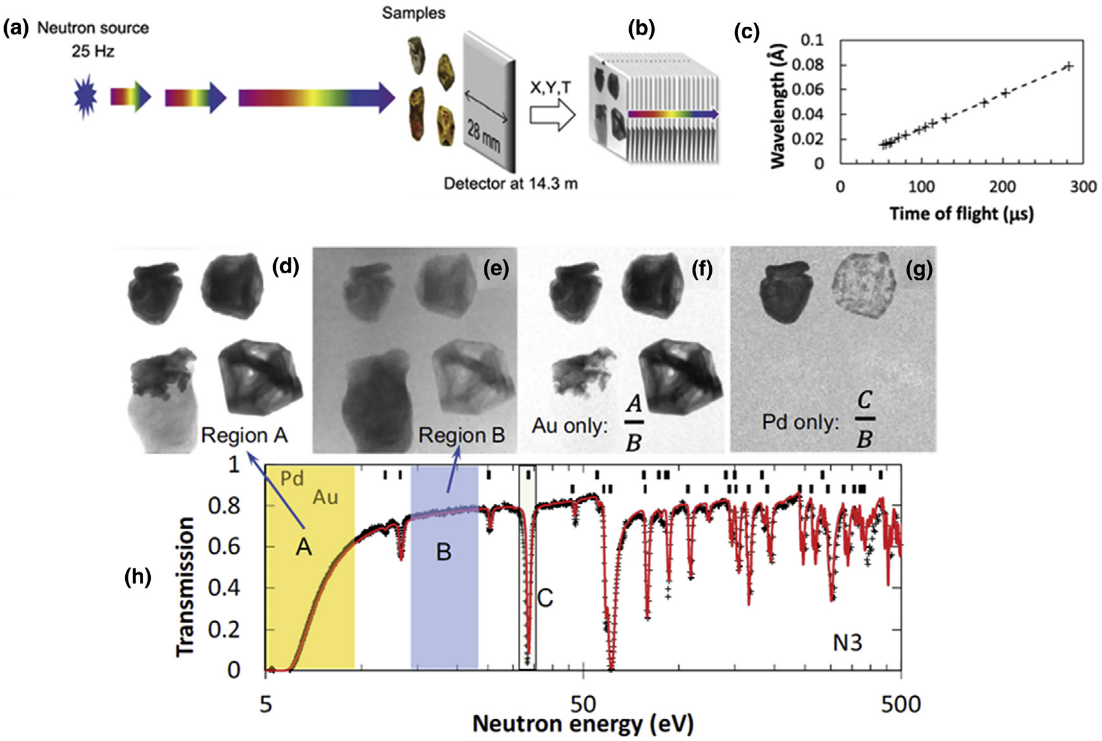

FIGURE 6

Schematic diagram of an experimental setup at a pulsed neutron source. (a) Neutron pulses travel from the source toward the sample and detector, which measures position *X*, *Y* and time *T* (determined relative to the time of spallation) for each registered neutron. (b) The result is a set of neutron transmission images, each corresponding to a specific neutron energy. (c) Calibration providing the relation between the time of flight and the corresponding wavelength. Energy-specific neutron transmission images allowing for a mapping of elemental distributions. (d) Transmission image obtained at the energies of the gold resonance of spectral region A in the spectrum (h). (e) Transmission measured at energies B with no resonances present for these samples. (f) Image (d) normalized by image (e), emphasizing the contribution of gold only. (g) Image measured at the Pd resonance energy (spectral region C) normalized by an off-resonance in region B, emphasizing the distribution of Pd within the samples. No Pd is detected in the two bottom samples [158].

configuration of the intermediate stress states are shown in Fig. 8c where the original domain structure of the coated state is reproduced at a stress value of 20 MPa. Furthermore, the example shows how the applied stresses lead to a refinement of the volume domain structure and the suppression and reoccurrence of supplementary domains [52].

Neutron grating interferometry has also been used for fundamental investigations of the magnetic properties of superconducting materials such as niobium [54]. Nb is a type-II superconductor in which at certain external magnetic field B_{C2}, the Meißner-Ochsenfeld effect that is characterized by an expulsion of the field from the interior of the superconductor, is broken and the field starts to penetrate the sample volume in form of a vortex lattice (VL) as shown in Fig. 8. This is the so-called Shubnikov phase. However, for materials with a low Ginzburg–Landau parameter k such as niobium [165], the transition from the Meißner to the Shubnikov phase at the lower critical field (H_{C1}) is characterized by a discontinuity in the intervortex lattice spacing d_{VL}. In samples with a non-zero demagnetization coefficient N, an intermediate mixed-state (IMS) phase is formed in which isolated Shubnikov domains with a typical diameter d_{IMS} are nucleated, surrounded by the field-free Meißner state. Fig. 8b shows a generic *B*–*T* phase diagram of Nb as well as a schematic depiction of the IMS and Shubnikov phases including their characteristic length scales d_{VL} and d_{IMS}, respectively, Fig. 8c and d. By neutron grating interferometry, being sensitive to the micrometer length scales on which the IMS domains are formed, it is possible to obtain spatially resolved maps of the IMS bulk domain distribution, hence, local information becomes visible as shown in Fig. 8e.

The results are grouped in transmission images (TI) in the top row and dark-field images (DFI) in the bottom row. The TI provides information about the local structure of the VL by showing where the angle enclosed by the incoming neutrons and the orientation of the VL fulfills the Bragg condition. Hence, neutrons that are locally scattered away from their original direction lead to a decrease of the intensity at the corresponding position on the detector. The DFI provides spatially dependent information on domain formation of the VL namely the IMS phase. The signal is caused by neutrons that lose their coherence due to ultra-small-angle scattering at the IMS domains with diameters in the μm range.

Magnetic properties of materials can also be investigated by utilizing the magnetic moment of the neutron more directly via its interaction with an incident polarized beam [7,166–171]. The magnetic moment is antiparallel to the internal angular momentum of the neutron described by a spin *S* with the quantum number $s = 1/2$. The high sensitivity of neutrons to magnetic interactions has been exploited in numerous experiments aiming at understanding fundamental magnetic

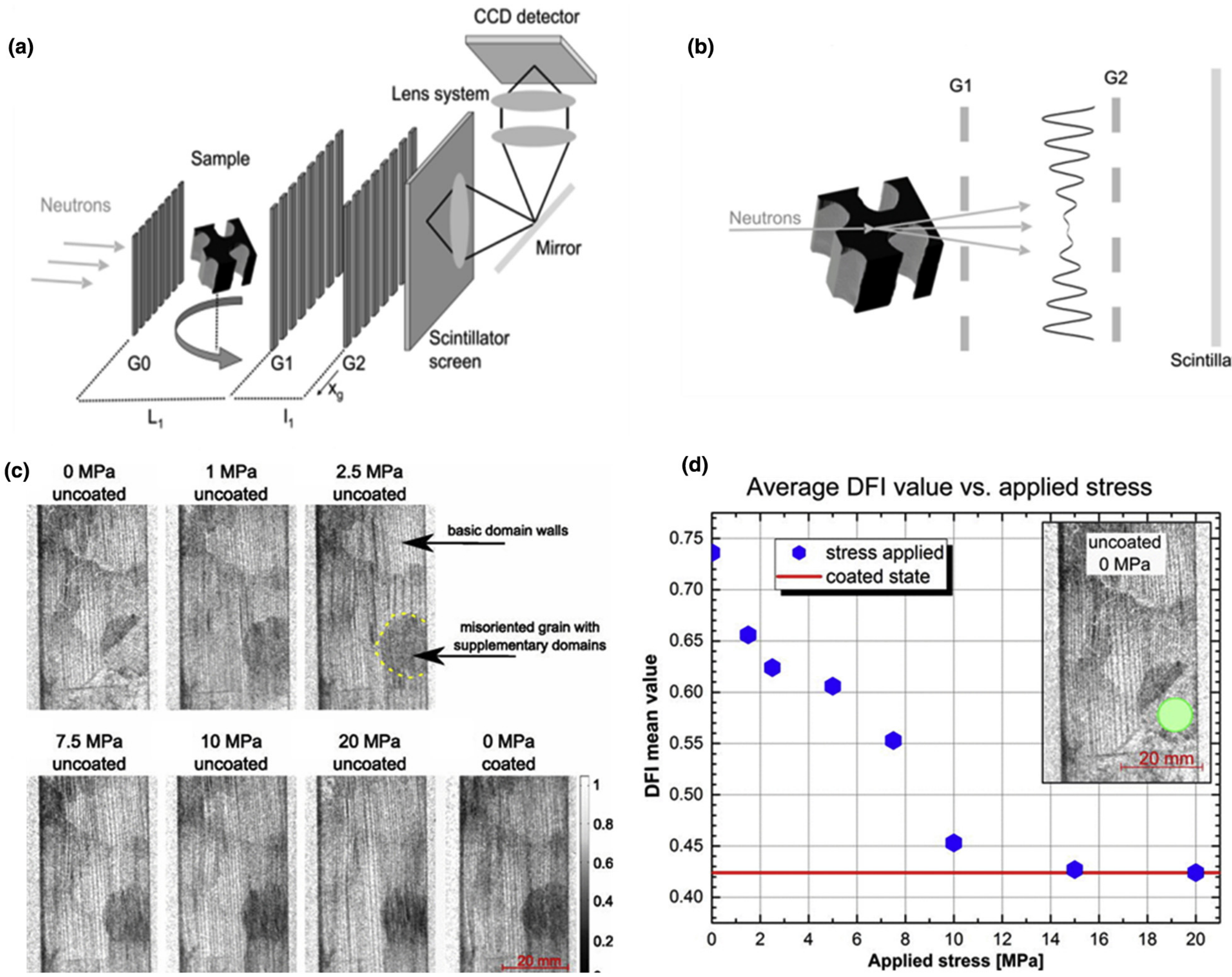

FIGURE 7

(a) An incoming neutron beam first passes a grating (G0), which produces many partial coherent sub-beams that after passing the sample give rise to an interference pattern behind the next phase grating (G1). The structure of this pattern is much finer in detail than the spatial resolution of the imaging detector and can be resolved only by applying a further analyzer grating (G2) that is scanned in the transverse direction. (b) The presence of a sample distorts the interference pattern locally and this distortion is now encoded in the detector signal. (c) The first state: uncoated high-permeability steel laminates (HPSL) without applied external stress. Increasing applied stresses up to 20 MPa lead to a refinement of the volume domain structure, the suppression of grain boundary domains at grain boundaries, and a re-occurrence of the domain structures in the misoriented grain. Final state: coated HPSL without applied stress. (d) Stress-dependent supplementary domain formation in the misoriented grain (area marked by the green circle in the inset) measured by dark-field images. The dark-field imaging value for the coated state (red line) is reproduced at 20 MPa applied stress [52].

properties and basic phenomena in condensed matter. For the imaging setup, a polarizer and analyzer are used to select a defined neutron polarization or orientation of the magnetic moment as shown in Fig. 9a and to convert the precession angle of the neutron spin after transmission through the magnetic field or sample to imaging contrast, respectively. The method is applicable for the visualization of small magnetic fields (few mT) with a limited spatial resolution (100 μm). An example for this is the visualization of trapped magnetic field in a bulk YBaCuO (YBCO) superconductor [171] at different temperatures below T_c, Fig. 9b.

Quantification of the magnetic field in 3D is another task that can be solved using polarized neutrons. The measurement of beam depolarization in a sample for each of the three orthogonal spin components X, Y, and Z provides a set of projections which can be used for an iterative process of computation modeling of the obtained result, Fig. 9d, and allows for a tomographic reconstruction of the magnetic field produced by a sample as seen in Fig. 9e.

In addition to this iterative approach, new algorithms for the reconstruction of the magnetic field tensor in 3D are under development [172].

Soil–root systems and geomaterials

The development of new methods and innovative instrumentation in the field of conventional absorption-based neutron radiography and tomography can be exploited to understand not only problems in materials science and technology but also in biology, medicine, archeology and paleontology. For example, the development of ultra-fast tomography allows for acquiring full volume data sets in just 10 s. This has been a crucial factor in several studies of plant physiology and problems in geosciences.

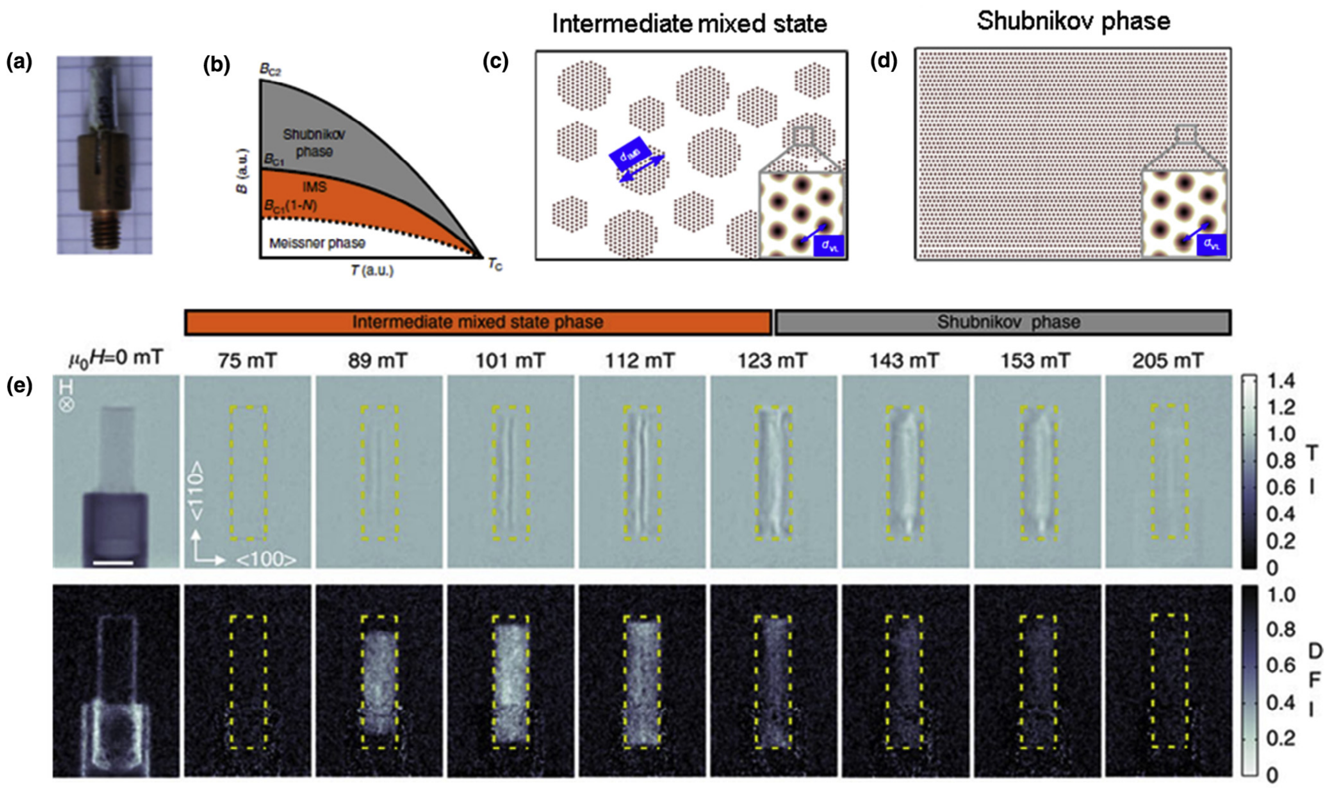

FIGURE 8

Schematic B–T phase diagram of a niobium rod. (a) Image of the Nb rod investigated in this study. (b) Generic phase diagram of the sample: because of the non-zero demagnetization coefficient *N* of the Nb rod, an IMS phase emerges in fields $Bc_1(1 - N) < B < Bc_1$. The corresponding schematic drawings of the (c) IMS phase and (d) Shubnikov phase show the characteristic length scales of the intervortex lattice distance d_{VL} and IMS domain size d_{IMS}. (e) Transmission and dark-field images of an ultra-pure niobium rod as a function of magnetic field. The magnetic field was successively increased after zero-field cooling to $T = 4$ K. The contour of the sample is indicated by the yellow dashed boxes. The scale bar shown in (e) is 5 mm long. The transmission images (TI, top row) and dark-field images (DFI, bottom row) results for $B > 0$ are normalized by the results at $\mu_0H = 0$ mT, hence only the pure magnetic contribution from the VL is visualized. The TI and the DFI provide information about the flux line lattice within the vortex domains and the VL domain formation in the IMS phase, respectively [54].

The 3D visualization of water uptake by plants [173–175] helps us to model and understand the interaction between soil and plants much better than in previous 2D studies [176,177]. In order to track the water movement in soil, heavy water (D_2O) was used as a contrast agent since it is distinguishable from natural water due to its smaller attenuation coefficient for neutrons. An example for such an ultrafast tomography series in which D_2O was used as a tracer is presented in Fig. 10a [174]. One can resolve the displacement of the initially present natural water at the bottom of the container and in the very small pores, the size of which is under the resolution limit of the detector system by the injected D_2O. The natural water moves upward in a sharply defined front and eventually interacts with the roots.

This advance in neutron tomography can be used to study similar problems in other research areas such as, for example, water penetration into rocks or sand. Another development is the combination of neutron and X-ray imaging using the same pixel size that allows for a comparison and even matching of tomographic slices and volumes. In the following example, partially water-saturated compacted wet sand specimens were characterized by both neutron and X-ray tomography. The resulting data was combined to a single composite image, Fig. 10b [178]. Neutron and X-ray images provide complementary information and allow one to precisely identify the three phases in the compacted sand specimens, namely silica sand, air, and water. Neutron tomography provides high contrast for the water phase possessing higher attenuation coefficient than the silica sand and the air, whereas X-ray tomography clearly depicts the silica sand phase. This technique has been used in several studies [179–182]. In the example given here, coordination numbers (number of point contacts of a sand grain with neighboring grains) and pore size distributions provided information about the fabric of the system, Fig. 10c. Partially water-saturated specimens were prepared from sands featuring two different grain shapes (rounded Ottawa sand and angular Q-Rock sand), and the effects of different grain shapes on water distribution and fabric were studied, Fig. 10 d.

Neutron imaging is also ideally suited to study the water uptake and distribution in other geomaterials [183] such as porous rocks [184,185]. Internal stresses in such systems can be studied by volumetric image correlation [186].

Teeth and bones

Neutron imaging in medicine has mainly focused on problems related to teeth and bones up to now. The example shown in Fig. 11a and b shows a study of different cement materials used

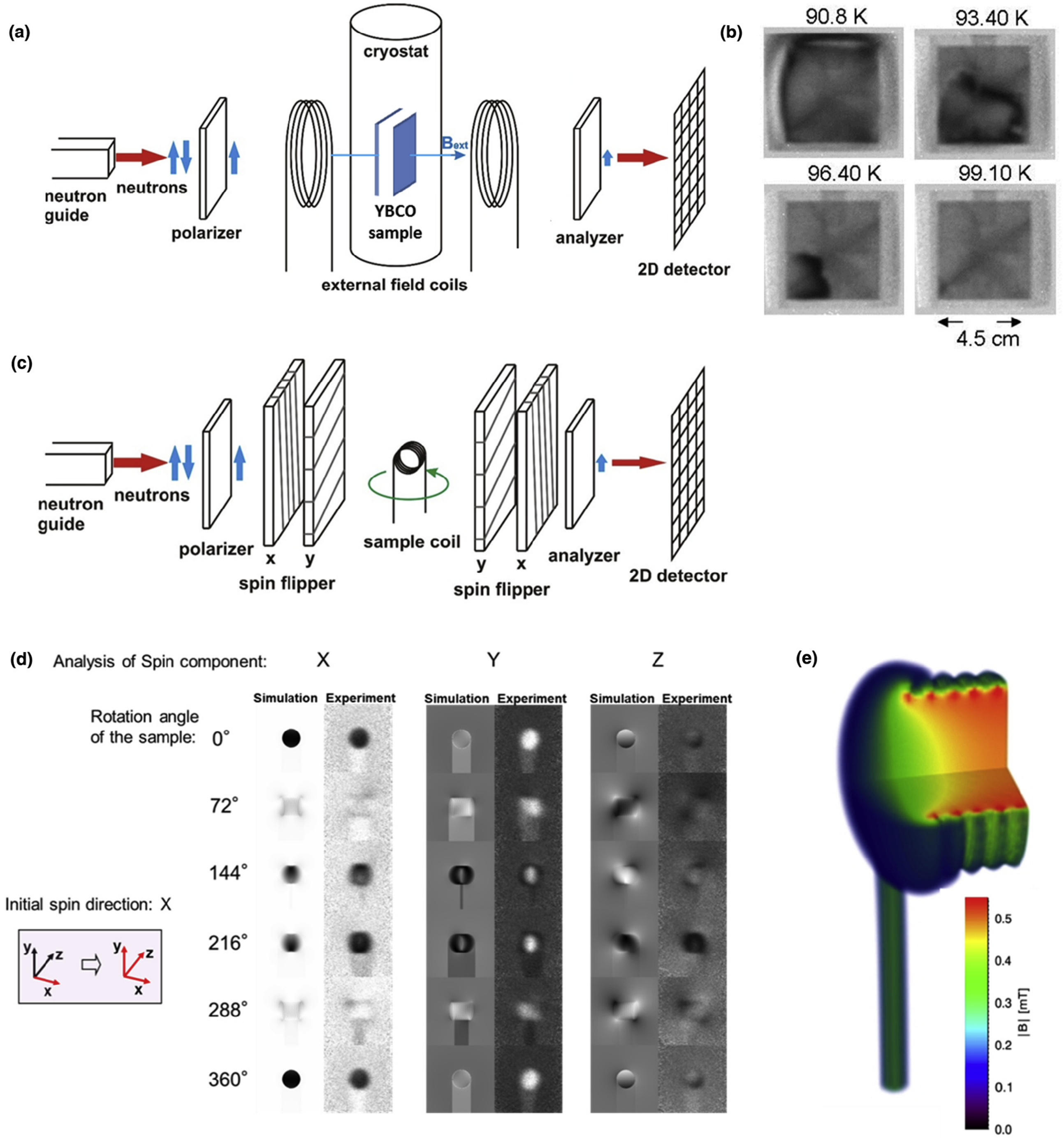

FIGURE 9

(a) Principle of imaging with polarized neutrons. (b) Visualization of trapped magnetic field in bulk YBCO superconductor ($45 \times 45 \times 12$ mm^3) using polarized neutrons. The magnetic field causes a spin precession which gives rise to reduced neutron transmission through the analyzer and is seen as dark contrast in the images. This helps to visualize the distribution of the field in the superconductor [171]. (c) Principle of the experimental arrangement for polarimetry. (d) Quantification of the magnetic field produced by a current solenoid using neutron polarimetry. The angular projections were simulated using Biot-Savart's law. After iterative tuning of the current in the coil, good agreement with the experiment was achieved. (e) These simulated projections were used for the iterative 3D reconstruction of the magnetic field distribution produced by the coil [172].

for dental tooth recovery where by X-ray tomography the macroporosity in the inlay material can be visualized, while the neutron images provide information about the hydrogen distribution in the cement and even indicate that some pores are filled with liquid [22]. Such a combination of the two imaging techniques can be carried out at some neutron beam stations (e.g., NEUTRA@PSI, ANTARES@FRM-2, NIF@NIST and CONRAD-2@HZB) [187–190] that provide integrated X-ray imaging facilities in addition to neutron imaging.

Teeth and bones are commonly investigated by X-ray tomography but the presence of metallic components (gold, titanium etc.) may induce artifacts due to strong absorption. Neutron

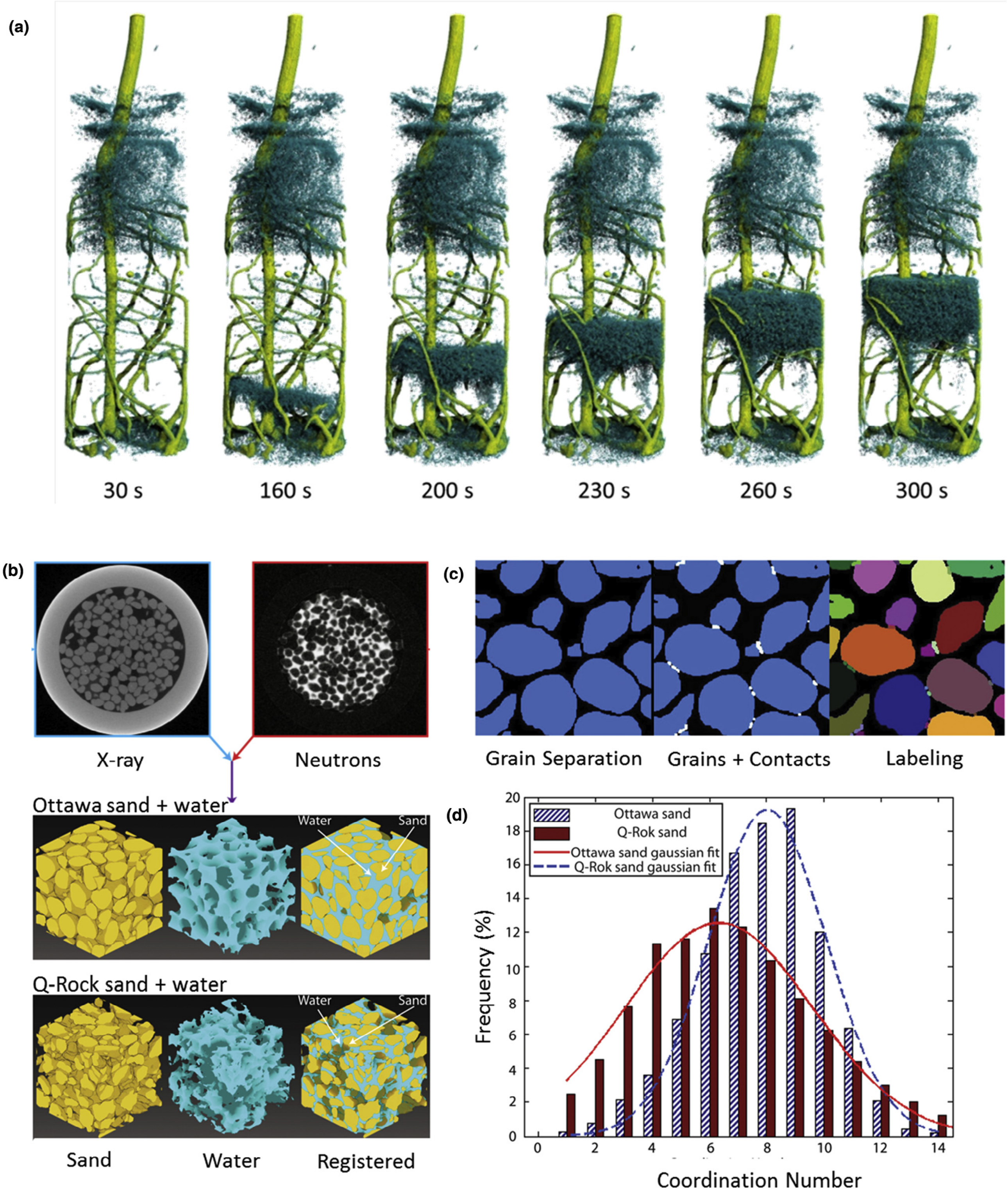

FIGURE 10

(a) Time-resolved neutron tomography of the root system of a lupine after the injection of 4 ml deuterated water (D_2O) through the bottom. The time series ($30\text{ s} \leq t \leq 300\text{ s}$) shows the ascending front of water (H_2O) moving upward as it is being displaced by the injected deuterated water. The repetition time for the tomograms is just 10 s [174]. (b) Illustration of the creation of composite images based on tomographic slices representing both neutron and X-ray volumetric data. Composite images for both wet Ottawa and Q-Rock sand specimens are shown. (c) Illustration of the procedure applied to compute the coordination numbers of individual particles. (d) Coordination number distribution for both wetted Ottawa and Q-Rok sand [178].

tomography is a promising alternative in such cases and can be used, for instance, to characterize in-situ the response of bone-implant interfaces to mechanical loading. Experiments were performed in which metal screws were inserted into rat tibiae during 4 weeks, Fig. 11c [23,24]. The screws were pulled-out while the samples were sequentially imaged in-situ by neutron tomography. The images were analyzed to quantify bone ingrowth around the implants. The neutron images were free of metal-related artifacts, which enabled an accurate quantification of bone ingrowth on the screw (ranging from 60% to 71%). Digital Volume Correlation (DVC) was used to track the internal displacements and calculate the strain fields in the bone during loading, Fig. 11d. DVC allowed for a successful identification of the deformation and cracking that occurred during mechanical loading and led to final failure of the bone-implant interface, Fig. 11e.

Even the structure of soft bones in fossilized dinosaur skulls can be revealed due to the high penetration power of neutrons that easily transmit bulky rock samples and provide good contrast for the hydrogen contained in such fossilized bones. In the example shown in Fig. 11f, software tools were applied to the phase segmentation of the bone structure and allow us to extract fine details from the nasal cavity of the skull. The analysis points at an endothermic metabolism of Lystrosaurus declivis (Therapsida, Anomodontia). In this way, it was possible to conclude that the investigated dinosaur species were warm-blooded animals [25].

Materials in cultural heritage artifacts

Diffraction contrast, which was introduced in chapter 4 of this article, can also be exploited for a non-destructive evaluation of metallic cultural artifacts [31,32,191–196]. The study from which an example is taken and presented in Fig. 12a and b was

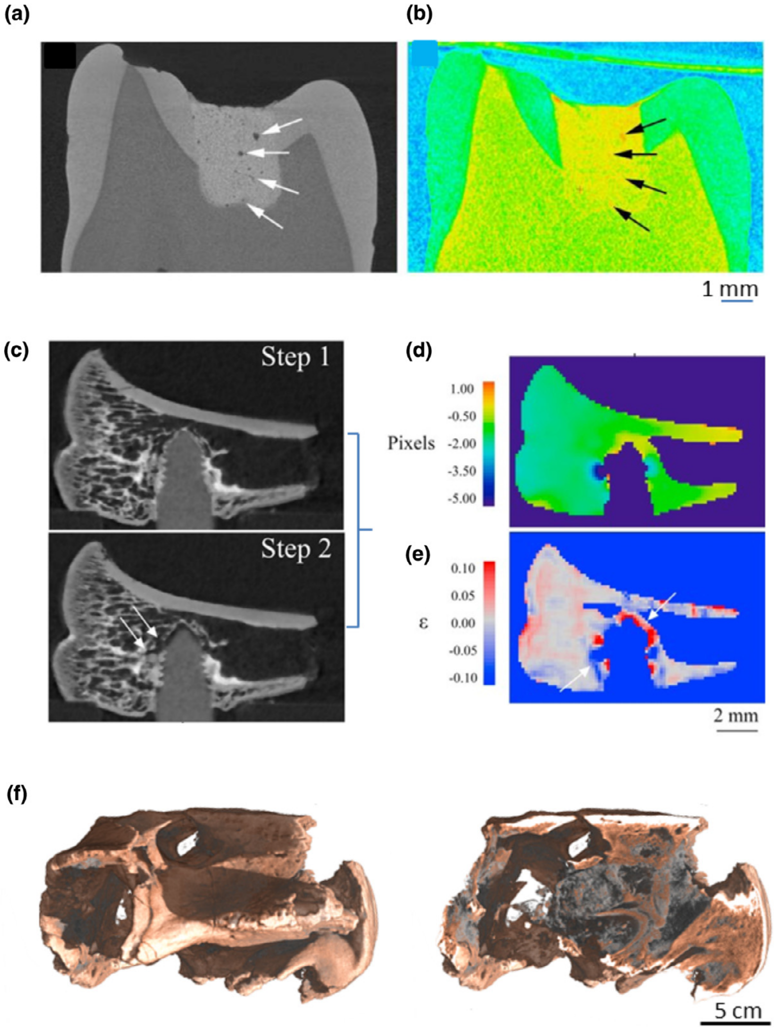

FIGURE 11

(a and b) An example from dentistry shows an extracted tooth restored with glass ionomer cement (GIC). (a) Pores and cracks are better visible in the X-ray images due to the superior resolution. (b) The presence of liquid inside or adhered to the internal walls of some of the larger pores is evident (in red, due to the higher attenuation coefficient of hydrogen) in the neutron image. The neutron image also suggests that interconnecting pores or cracks are filled with liquid [22]. (c–e) Bone sample (rat tibiae) treated by bone morphogenetic protein 7 (BMP7) with implanted titanium screw in a sagittal view. (c) Image cuts for two loading steps: one at initiation of loading (top) and one loaded (bottom), the white arrows localizes the crack. On the right, Digital Volume Correlation results between the two loading steps with (d) Z-displacements and (e) volumetric strains, the white arrows localize positive strains close to the tip of the screw and negative strains where a piece of bone had detached [24]. (f) Neutron tomography of a skull of Lystrosaurus declivis (Therapsida, Anomodontia) from the Lower Triassic from South Africa. The result shows complexly constructed nasal cavity, which provides evidence that Lystrosaurus was already endothermic. The endothermic metabolism allowed Lystrosaurus to tolerate high ambient temperature fluctuations [25].

concerned with the microstructural characterization of Japanese sword blades representing five Koto age (A.D. 987–1596) sword-making traditions [191]. Using a mechanical velocity selector for beam monochromatization, two neutron wavelengths before (3.8 Å) and after (5.0 Å) the Bragg-edge for carbonized steel were chosen and used to perform tomography measurements. Post processing procedure was used to subtract the image stacks – the one measured at 5.0 Å from the one measured at 3.8 Å. In this way, the absorption-based attenuation is canceled out and in the resulting image stack the contrast is based on diffraction only. The image stack so obtained allows for a 3D phase analysis in the carbonized steel of the blades. This information provided insights into the manufacturing process and gave hints about the development of metallurgy and craftsmanship in Japan in the Middle Ages.

The tomographic slices taken from Fig. 12a suggest that the investigated blade related to the Sashu sword making tradition has probably been manufactured by assembling a "jacket" (side and back) of low-carbon steel (*shingane*) around a very hard steel (the so-called *hagane*) composing the core and the edge of the sword. This allows one to identify the present configuration and assign the sword to one among the *Orikaeshi Sanmai*, *Soshu Kitae*, *Wariha Tetsu* or *Honsanmai* configurations. As it is apparent from the tomography slices shown in Fig. 12b, the other samples, namely S0, S2, S3, and S8 are also characterized by a structure similar to that of S7, with an outer soft-steel jacket (side and back of the blades) wrapped around an inner hard-steel core and edge.

Another example showcasing the unique capabilities of neutron imaging regarding penetration power and attenuation contrast is presented in Fig. 12c–f, where a sculpture made of lead has been investigated by neutron tomography [197]. The aim was to assess its present state of conservation and reveal the unknown manufacturing techniques used by the artist and the materials contained in the sculpture. The name of the sculpture is "The Violinist". It was made by Spanish sculptor and painter Pablo Gargallo in 1920 using a wooden core and lead sheets nailed onto it, Fig. 12d. In its present state, the metal is corroded by carbonation, most likely under the influence of organic substances released by the wooden core, Fig. 12e. The urgently necessary conservation of the artifact requires a strategy how the sculpture could be taken apart in order to enable treatment of the lead carbonate crusts on the inner surface of the lead sheets by a hydrogen plasma, which has been tested and proved to be an effective treatment method. The results of the study are presented in Fig. 12f. They suggest appropriate strategies on how the sculpture could be disassembled at minimal risk. Having information in advance about the condition inside the sculpture will also enable conservators to foresee the steps for future treatment.

Inspection of devices

Innovative analytic algorithms for image processing allow one to extract valuable information even in cases where the contrasts between the different components of the object investigated are very weak. An example of this is presented in Fig. 13, where in a diesel particulate filter from a truck exhaust system soot, ash and metal particles were separated from the monolithic body. The denoising of the high-resolution tomographic data (pixel size of 13 μm) allowed one to distinguish between the two carbon-based substances soot and ash and finally provide the quantitative morphological information needed for the optimization of the corresponding device [198,199].

Outlook on new developments: high-resolution neutron microscopes, imaging at spallation sources and other novel techniques

Significant progress regarding spatial and temporal resolutions in neutron imaging is evident and can be seen from the examples presented in this article. Nonetheless, the majority of applications would greatly benefit from further improvements and work is under way to achieve these.

Major improvements regarding spatial resolution have already been achieved for the most commonly used imaging detector system consisting of a scintillator screen and an optical camera. By introducing magnifying optics behind the scintillator screen, optimizing scintillator screens and also using improved cameras, resolutions below 10 μm are already possible [35,37] and continue to improve. Another approach aims at the use of focusing optics for neutrons, namely grazing-incidence mirrors based on full figures of revolution (often referred to as Wolter mirrors) [200], which can be used for magnifying objects in the imaging mode when the sample is placed before the optic [201], but also for improved intensities in imaging and small angle neutron scattering experiments when the sample is placed behind the optic [202]. Such devices could transform neutron imaging instruments from pinhole cameras into microscopes. Another interesting development, which principally could lead to high gain factors in terms of temporal and spatial resolution, concerns imaging with coded apertures as applied in optical astronomy, where spatial multiplexing is used and in principal bears the advantage of higher efficiencies since several point sources are used simultaneously [203], but no convincing applications could yet be demonstrated.

One key factor for the recent surge of successful applications in multidisciplinary fields lies in the fact that novel contrast mechanism are now routinely being utilized in advanced imaging setups. Many of these techniques rely on the possibility to perform energy-resolved measurements. At steady-state sources, this is typically achieved by tuneable double-crystal monochromators or mechanical velocity selectors that select a given wavelength for each measurement [42,43,204,205] or alternatively using choppers [140,206]. They all allow for a continuous coverage of a certain wavelength range. Most efficiently, however, wavelength–dispersive measurements can be performed at spallation sources, where time-of-flight techniques can be utilized without any further effort. The successful applications relying on wavelength-resolved measurements have, as already mentioned in the introduction of this article, triggered the development of neutron imaging instruments at powerful spallation sources that are now been installed [56–58] or are under construction [59,60].

While some of the relatively new methods have matured enough to attract academic and industrial users, other advanced techniques are still under development. Especially imaging in

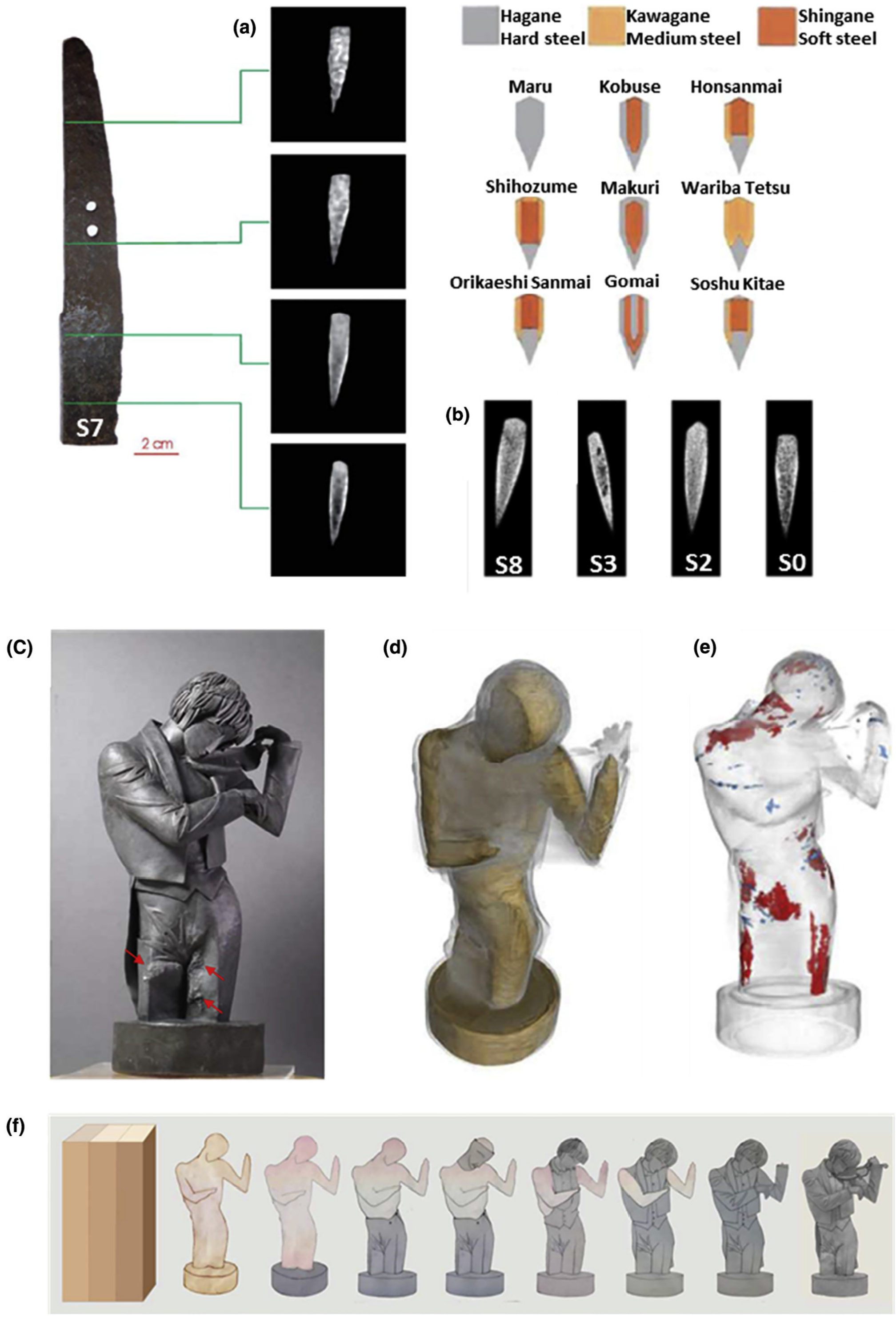

FIGURE 12

(a) Reconstructed slices at different positions of the swords. In the resulting image stack after subtraction of tomography volumes measured at 5.0 Å from one measured at 3.8 Å it is possible to distinguish light areas of ferrite and dark areas of cementite. On the right, some typical Japanese sword configurations based on steels of different carbon contents are shown. (b) Selected slices of energy-resolved tomographies show areas of different types of steel: the lighter soft "jacket" and the darker hard "core and "edge of the blade [191]. (c) Photo of the current state of the sculpture "The Violinist (1920) made by Pablo Gargallo using lead sheets. Corroded areas are marked by red arrows. (d) 3D neutron tomography reconstruction of the sculpture showing an inner wooden core. (e) Mapping showing corroded areas (in red) inside the lead sheet, remains of flux and nails (blue) according to the information given by the tomograms. (f) Hypothetical steps followed by Gargallo during the construction of The Violinist. The same steps in reverse sequence can be used for disassembling the sculpture [197].

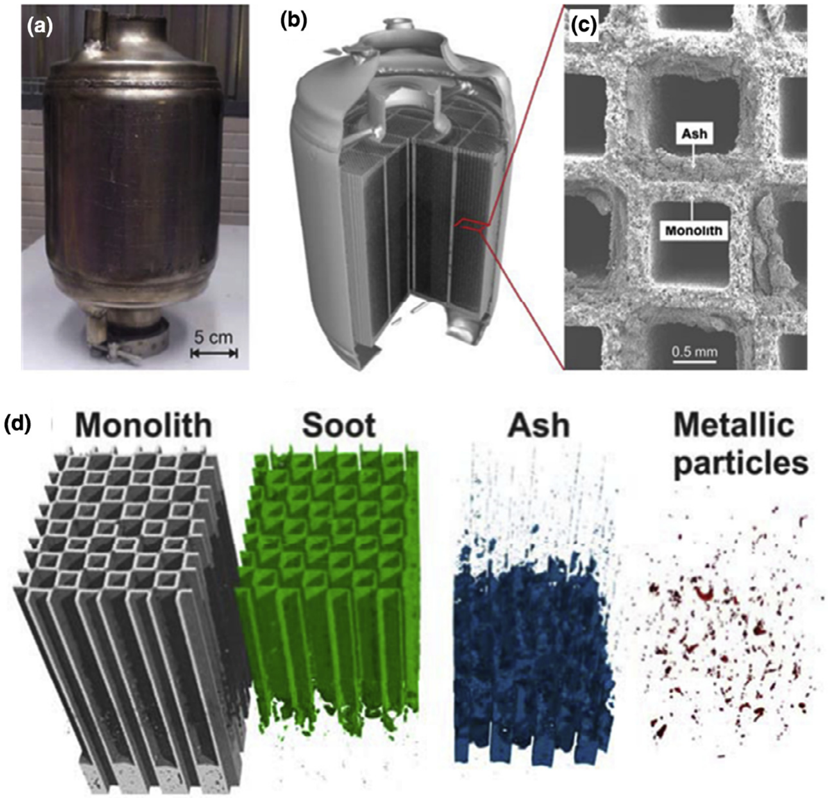

FIGURE 13

(a) Photograph of the canned diesel particulate filter. (b) Neutron tomography data. The steel jacket is no barrier for neutrons and allows for an insight into the loaded monolith. (c) Scanning electron micrograph showing the soot layer with a thickness of 250 μm on the filter wall surface. (d) High-resolution neutron tomography: Segmentation of the individual components of the sample [198,199].

the ToF mode at spallation sources will enable completely new and unprecedented possibilities, but at the same time still poses challenges regarding available detector technologies (requiring a combination of spatial and time resolution, a large field of view and the capability to cope with high count rates) and efficient data analysis.

Diffraction contrast occurring due to Bragg scattering from crystal lattice planes is routinely being exploited at steady state and spallation sources to visualize phase differences and to reveal textural heterogeneities both in engineering samples and cultural heritage artifacts. In certain cases, strain maps obtained via Bragg edge profiles readily provide invaluable insights (see e.g., Fig. 5d and e), while the extension to quantitative strain tensor mapping is still being investigated [207–214].

It should be emphasized that acquired transmission images are always integrals along beam trajectories through a sample and angular information regarding the diffracted beam (normally detected in diffraction experiments) is lost, which leads to complications for single crystals and textured materials when it comes to an unambiguous interpretation.

There are several approaches to carry out imaging in the diffracted beam geometry such as neutron topography, where the detector is moved into a Bragg reflection of a single crystal or a large crystal grain in the vicinity of a sample [215–218] and also topo-tomography [219]. Tomographic reconstructions with limited spatial resolution (~3 mm) can also be carried out using the off-center sample displacement in diffraction experiments and was demonstrated for the determination of phase compositions [220]. Recent approaches at steady-state sources also aimed at reconstructing the grain morphology and grain orientation in polycrystalline samples [221] where – in contrast to topography of single crystals – a compromise has to be found between a short sample-to-detector distance for high spatial resolution and a long sample-to-detector distance to avoid overlap of the diffracted beam from different grains. Limitations for most of these approaches include very long measurement times that could be overcome when performed in the ToF mode at spallation sources. Most recently, first results from a spallation source were presented, where the morphology of >100 individual grains was reconstructed based on a transmitted beam alone ('extinction spot analysis') [222,223] while ongoing efforts aim for combining this information with simultaneously recorded diffraction signals from grains ('diffraction spots analysis'). The efforts could eventually enable an unambiguous and quantitative 3D phase mapping in textured materials, texture mapping by locally resolved Orientation Distribution Functions and even strain tensor tomography.

As depicted in Fig. 6, information can even be obtained regarding the elemental composition of many materials through resonance absorption imaging (NRAI), where individual isotopes of each element absorb neutrons of defined energies. This absorption in return causes an excitation of nuclei, resulting in the emission of several gamma-ray photons as they return to their ground state. Several examples demonstrate the usefulness of NRAI alone [224–227], even allowing to measure gas pressures [228], while some applications make simultaneous use of information and analysis that is available in such experiments [229,230]. Such an example is presented elsewhere [230], where several dissimilar welds were investigated by ToF imaging. Here, NRAI provides the elemental composition and allows for analyzing diffusion between welding zones, while analysis of Bragg edges provides insight into texture variations in the plate material, the extent of the heat-affected zone and re-crystallization and allowing for mapping the residual strain distribution in the through-thickness direction.

As the examples in Fig. 7 show, neutron grating interferometry [6,46,47] decouples angular and spatial resolution and allows for detecting phase contrast (shift of phase due to refraction) and dark-field contrast (due to small-angle scattering) in addition to attenuation contrast, thus allowing one to reveal structure sizes below the detector resolution. Many applications have utilized grating interferometry to gain insights into the microstructure of engineering materials [231] and to visualize magnetic domains both in 2D [51–55] and in 3D[10]. The contrast information obtained in these studies, however, mainly allows one to distinguish between the strength of scattering, without further quantifying the dark-field signal itself. Recently, a general theoretical solution for image formation in dark-field images has been introduced [48], allowing for extracting quantitative real-space correlation functions that are, for example, typical for Spin-echo small-angle neutron scattering (SESANS) [232] measurements for every pixel, i.e., enabling SANS with simultaneous image resolution. It was experimentally shown that this can be achieved by scanning the wavelength over a certain range [233] or using a modified neutron grating interferometer that images in the third Talbot distance and scanning the sample at the G2 distance – between the phase and analyzer gratings [234]. Potential applications are manifold, e.g., crystallization processes, biological systems, inclusions and porosities in a variety of materials beside many other applications where microstructure variations occur at macroscopic length scales. Another experimental approach that allows for quantitative dark-field imaging is also based on beam modulations, but not by a grating setup but instead using a spin-echo approach. It is referred to as spin-echo modulated SANS (SEMSANS) [235–238] This approach is more flexible and overcomes some limitations of the grating interferometer (such as that the gratings are optimized for a certain wavelength, the limited scanning range of the sample-to-detector distance) and can straight forwardly be applied in the time-of-flight mode to probe the real-space correlation length in a wavelength-dispersive approach. The resolvable microscopic size ranges that give rise to the dark-field signal – in so far realized experimental setups – are typically in the range of 10–400 nm for SEMSANS and 1–4 μm for the grating interferometer, implying a complementary of the approaches allowing for bridging information across many length scales with neutron imaging. Other imaging modalities, such as Bragg edge analysis can still be performed simultaneously and hence it can be envisaged that such multimodalities will become a very attractive tool at powerful spallation neutron sources.

Summary

We review some of the most recent developments in the field of neutron imaging and pick various different application examples that represent current research in different fields. In the past years, 2D and 3D neutron imaging techniques have become versatile tools in a wide range of materials research and engineering. Because the techniques are non-destructive and non-invasive they allow for in-situ and operando measurements. The range of applications includes most large research areas ranging from civil engineering to energy-materials research, geology and plant research to fundamental physics and magnetism, while neutron imaging techniques are also of increased importance in medical research, archeology, and paleontology.

The introduction of novel imaging techniques together with unprecedented improvements in spatial resolution and measurement speed have been the main driving factors for this development. Neutron imaging techniques that employ contrast mechanisms beyond conventional attenuation contrast are no longer exotic methods restricted to a small specialized community but have rather become standard imaging tools at most neutron imaging facilities and are widely used by materials researchers.

A fast growing community of researchers is discovering neutron imaging as a powerful tool for their research. With the previously mentioned further technical improvements and optimizations and the introduction of modern spallation sources we expect this trend to continue in the future.

References

[1] J.M. Carpenter, C.-K. Loong, Elements of slow-neutron scattering, Cambridge University Press, 2015.
[2] J. Banhart, Advanced Tomographic Methods in Materials Research and Engineering, Oxford University Press, Oxford, UK, 2008.
[3] N. Kardjilov et al., Mater. Today 14 (6) (2011) 248.
[4] C.W. Clark et al., Nature 525 (7570) (2015) 504.
[5] F. Pfeiffer et al., Phys. Rev. Lett. 96 (2006) 21.
[6] M. Strobl et al., Phys. Rev. Lett. 101 (12) (2008) 123902.
[7] N. Kardjilov et al., Nat. Phys. 4 (5) (2008) 399.
[8] B.E. Allman et al., Nature 408 (6809) (2000) 158.
[9] F. Pfeiffer et al., Nat Mater 7 (2) (2008) 134.
[10] I. Manke et al., Nat. Commun. 1 (2010) 125.
[11] C. Grunzweig et al., Appl. Phys. Lett. 93 (11) (2008) 112504.
[12] R. Woracek et al., Adv. Mater. 26 (24) (2014) 4069.
[13] R. Woracek et al., Nucl. Instrum. Methods Phys. Res., Sect. A 878 (2018) 141.
[14] C. Hartnig et al., Materials Testing-Materials and Components Technology and Application 50 (10) (2008) 609.
[15] I. Manke et al., Appl. Phys. Lett. 90 (21) (2007) 214102.
[16] I. Manke et al., ZfP-Zeitung 109 (2009) 35.
[17] P. Boillat et al., Electrochem. Commun. 10 (4) (2008) 546.
[18] E.H. Lehmann, et al., Neutron imaging methods for the investigation of energy related materials Fuel cells, battery, hydrogen storage and nuclear fuel, in: M. Ceretti, et al., (Eds.), Jdn 21 – Neutrons and Materials for Energy, (2015), Vol. 104.
[19] M. Arif, et al., Neutron imaging study of the water transport in operating fuel cells, in: FY 2006 Annual Progress Report, (2006), p. 875.
[20] D.S. Hussey et al., Tomographic Imaging of an Operating Proton Exchange Membrane Fuel Cell, Destech Publications Inc., Lancaster, 2008, p. 470.
[21] L. Gondek et al., Int. J. Hydrogen Energy 36 (16) (2011) 9751.
[22] A.R. Benetti et al., Sci. Rep. 5 (2015) 8972.
[23] H. Isaksson et al., Bone 103 (2017) 295.
[24] S. Le Cann et al., J. Mech. Behav. Biomed. Mater. 75 (2017) 271.
[25] M. Laaß et al., Acta Zool. 92 (4) (2011) 363.
[26] F. Witzmann et al., Zool. J. Linn. Soc. 160 (2) (2010) 302.
[27] C. Zanolli et al., Physics Procedia 88 (2017) 109.
[28] M. Laaß, B. Schillinger, Physics Procedia 69 (2015) 628.

[29] M. Laaß et al., J. Morphol. (2017).
[30] N. Kardjilov, G. Festa, Neutron Methods for Archaeology and Cultural Heritage, Springer, 2016.
[31] D. Mannes et al., Insight-Non-Destr. Test. Condition Monit. 56 (3) (2014) 137.
[32] N. Kardjilov, Notiziario: neutroni e luce di sincrotrone 13 (2) (2008) 6.
[33] W. Kockelmann et al., Appl. Phys. A Mater. Sci. Process. 83 (2) (2006) 175.
[34] A.J. Brooks et al., Progr. Addit. Manufact. 2 (3) (2017) 125.
[35] S.H. Williams et al., J. Instrum. 7 (02) (2012) P02014.
[36] N. Kardjilov et al., Nucl. Instrum. Methods Phys. Res., Sect. A 651 (1) (2011) 95.
[37] P. Trtik et al., Physics Procedia 69 (2015) 169.
[38] E.H. Lehmann et al., Nucl. Instrum. Methods Phys. Res., Sect. A 576 (2–3) (2007) 389.
[39] I.S. Anderson et al., Springer Science+ Business Media 200 (2209) (2009) 987.
[40] A.C. Kak, M. Slaney, Principles of Computerized Tomographic Imaging, Society for Industrial and Applied Mathematics, 2001.
[41] M. Strobl et al., J. Phys. D Appl. Phys. 42 (24) (2009) 243001.
[42] E.H. Lehmann et al., Nucl. Instrum. Methods Phys. Res., Sect. A 603 (3) (2009) 429.
[43] W. Treimer et al., Appl. Phys. Lett. 89 (20) (2006) 203504.
[44] R. Woracek et al., J. Appl. Phys. 109 (9) (2011) 093506.
[45] J.R. Santisteban et al., J. Appl. Crystallogr. 34 (3) (2001) 289.
[46] F. Pfeiffer et al., Phys. Rev. Lett. 96 (21) (2006) 215505.
[47] C. Grünzweig et al., Rev. Sci. Instrum. 79 (2008) 5.
[48] M. Strobl, Sci. Rep. 4 (2014) 7243.
[49] M. Strobl et al., Nucl. Instrum. Methods Phys. Res., Sect. A 605 (1–2) (2009) 9.
[50] B. Betz et al., Rev. Sci. Instrum. 86 (12) (2015) 123704.
[51] B. Betz et al., Phys. Rev. Appl. 6 (2) (2016) 024023.
[52] B. Betz et al., Appl. Phys. Lett. 108 (1) (2016) 012405.
[53] P. Rauscher et al., Sci. Rep. 6 (2016) 38307.
[54] T. Reimann et al., Nat. Commun. 6 (2015) 8813.
[55] C. Grünzweig et al., Appl. Phys. Lett. 93 (2008) 11.
[56] W. Kockelmann et al., Physics Procedia 69 (2015) 71.
[57] Y. Kiyanagi et al., Physics Procedia 43 (2013) 92.
[58] T. Shinohara, T. Kai, Neutron News 26 (2) (2015) 11.
[59] H. Bilheux et al., Physics Procedia 69 (2015) 55.
[60] M. Strobl, Physics Procedia 69 (2015) 18.
[61] A. Hilger et al., Opt. Express 23 (1) (2015) 301.
[62] W. Kockelmann et al., Nucl. Instrum. Methods Phys. Res., Sect. A 578 (2) (2007) 421.
[63] M. Strobl, Nucl. Instrum. Methods Phys. Res., Sect. A 604 (3) (2009) 646.
[64] Y. Kiyanagi et al., J. Instrum. 9 (07) (2014) C07012.
[65] M. Morgano et al., Physics Procedia 69 (2015) 152.
[66] A. Griesche et al., Acta Mater. 78 (2014) 14.
[67] A. Griesche et al., Physics Procedia 69 (2015) 445.
[68] K. Herbrig et al., J. Power Sources 293 (2015) 109.
[69] C. Pohlmann et al., J. Power Sources 277 (2015) 360.
[70] C. Hartnig, C. Roth, Polymer electrolyte membrane and direct methanol fuel cell technology, In Situ Characterization Techniques for Low Temperature Fuel Cells, Vol. 2, Woodhead Publishing Limited, 2012.
[71] R.J. Bellows et al., J. Electrochem. Soc. 146 (3) (1999) 1099.
[72] D. Kramer et al., Electrochim. Acta 50 (13) (2005) 2603.
[73] R. Satija et al., J. Power Sources 129 (2) (2004) 238.
[74] C. Hartnig et al., J. Power Sources 176 (2) (2008) 452.
[75] A. Forner-Cuenca et al., Adv. Mater. 27 (41) (2015) 6317.
[76] Z.J. Lu et al., ECS Trans. 58 (1) (2013) 315.
[77] M.P. Manahan et al., J. Power Sources 196 (13) (2011) 5573.
[78] M.P. Manahan, M.M. Mench, J. Electrochem. Soc. 159 (7) (2012) F322.
[79] R. Alink et al., J. Power Sources 233 (2013) 358.
[80] J. Haußmann et al., J. Power Sources 239 (2013) 611.
[81] M. Klages et al., J. Power Sources 239 (2013) 596.
[82] A.B. Geiger et al., Fuel Cells 2 (2003) 92.
[83] T.A. Trabold et al., Int. J. Heat Mass Transf. 49 (25–26) (2006) 4712.
[84] H. Markotter et al., J. Power Sources 219 (2012) 120.
[85] I. Manke et al., Appl. Phys. Lett. 90 (2007) 18.
[86] J.P. Owejan et al., Int. J. Hydrogen Energy 32 (17) (2007) 4489.
[87] S. Gossling et al., J. Power Sources 306 (2016) 658.
[88] J. Kaetzel et al., J. Power Sources 301 (2016) 386.
[89] P. Boillat et al., Electrochem. Commun. 10 (9) (2008) 1311.
[90] I. Manke et al., Appl. Phys. Lett. 92 (24) (2008) 244101.
[91] A. Schroder et al., Int. J. Energy Res. 38 (7) (2014) 926.
[92] A. Schroder et al., Int. J. Hydrogen Energy 38 (5) (2013) 2443.
[93] A. Schröder et al., J. Power Sources 195 (15) (2010) 4765.
[94] A. Schröder et al., Electrochem. Commun. 11 (8) (2009) 1606.
[95] T. Arlt et al., J. Power Sources 299 (2015) 125.
[96] P. Boillat et al., J. Electrochem. Soc. 161 (3) (2014) F192.
[97] K. Takanohashi et al., J. Power Sources 343 (2017) 135.
[98] M.G. Makowska et al., ECS Trans. 68 (1) (2015) 1103.
[99] M.G. Makowska et al., J. Appl. Crystallogr. 48 (2015) 401.
[100] J.P. Owejan et al., Electrochim. Acta 66 (2012) 94.
[101] F. Sun et al., Appl. Surf. Sci. 399 (2017) 359.
[102] B. Michalak et al., Sci. Rep. (2015) 5.
[103] L.G. Butler et al., Physics Procedia 43 (2013) 331.
[104] M. Kamata et al., J. Power Sources 68 (2) (1997) 459.
[105] N. Kardjilov et al., Nucl. Instrum. Methods Phys. Res., Sect. A 542 (1–3) (2005) 16.
[106] M. Lanz et al., J. Power Sources 101 (2) (2001) 177.
[107] K. Kino et al., Physics Procedia 69 (2015) 612–618.
[108] H. Zhou et al., ACS Energy Lett. 1 (5) (2016) 981.
[109] J.B. Siegel et al., J. Electrochem. Soc. 158 (5) (2011) A523.
[110] T.F. Fuller et al., J. Electrochem. Soc. 141 (4) (1994) 982.
[111] J. Nanda et al., J. Phys. Chem. C 116 (15) (2012) 8401.
[112] D. Goers et al., J. Power Sources 130 (1–2) (2004) 221.
[113] T. Knoche et al., J. Power Sources 331 (2016) 267.
[114] B. Michalak et al., Anal. Chem. 88 (5) (2016) 2877.
[115] M. Hofmann et al., J. Electrochem. Soc. 159 (11) (2012) A1827.
[116] V. Zinth et al., J. Electrochem. Soc. 163 (6) (2016) A838.
[117] G.V. Riley et al., ECS Trans. 25 (35) (2010) 75.
[118] L.G. Butler et al., Nucl. Instrum. Methods Phys. Res., Sect. A 651 (1) (2011) 320.
[119] T. Esaka, Ionics 10 (5–6) (2004) 358.
[120] M. Kamata et al., Denki Kagaku 63 (11) (1995) 1063.
[121] J.B. Siegel et al., J. Electrochem. Soc. 160 (8) (2013) A1031.
[122] S. Takai et al., Solid State Ionics 123 (1–4) (1999) 165.
[123] W.B. Zhang et al., J. Mater. Chem. A 5 (20) (2017) 9929.
[124] K. Sharma et al., PCCP 15 (28) (2013) 11740.
[125] K. Kino et al., Solid State Ionics 288 (2016) 257.
[126] O. Halpern et al., Phys. Rev. 59 (12) (1941) 981.
[127] E. Fermi et al., Phys. Rev. 71 (9) (1947) 589.
[128] S. Vogel, A Rietveld-Approach for the Analysis of Neutron Time-of-Flight Transmission Data Dissertation, Univ Kiel, Kiel, 2000.
[129] J.R. Santisteban et al., Appl. Phys. A Mater. Sci. Process. 74 (2002) s1433.
[130] A. Steuwer et al., Physica B 350 (1–3) (2004) 159.
[131] A. Steuwer et al., J. Appl. Phys. 97 (7) (2005) 074903.
[132] R. Woracek et al., Physics Procedia 69 (2015) 227.
[133] E. Dabah et al., J. Mater. Sci. (2016) 1.
[134] A. Steuwer et al., Physica Status Solidi A 185 (2) (2001) 221.
[135] J.R. Santisteban et al., Nucl. Instrum. Methods Phys. Res., Sect. A 481 (1–3) (2002) 765.
[136] A. Steuwer, Strain Determination and Imaging by Pulsed Neutron Transmission, University of Cambridge, 2002.
[137] K. Iwase et al., Nucl. Instrum. Methods Phys. Res., Sect. A 605 (1) (2009) 1.
[138] M. Boin, Developments Towards the Tomographic Imaging of Local Crystallographic Structures PhD Thesis, Open University, 2010.
[139] K. Iwase et al., J. Appl. Crystallogr. 45 (1) (2012) 113.
[140] M. Strobl et al., Nucl. Instrum. Methods Phys. Res., Sect. A 680 (2012) 27.
[141] A.S. Tremsin et al., Strain 48 (2012) 296.
[142] Y. Su et al., Mater. Sci. Eng., A 675 (2016) 19.
[143] J.R. Santisteban et al., Physica B 385–386 (Part 1) (2006) 636.
[144] H. Sato et al., Nucl. Instrum. Methods Phys. Res., Sect. A 651 (1) (2011) 216.
[145] M. Boin et al., J. Phys. Conf. Ser. 340 (1) (2012) 012022.
[146] N. Kardjilov et al., Int. J. Mater. Res. 103 (2) (2012) 151.
[147] J. Santisteban et al., J. Nucl. Mater. 425 (1) (2012) 218.
[148] F. Malamud et al., J. Appl. Crystallogr. 47 (4) (2014) 1337.
[149] F. Malamud, J.R. Santisteban, J. Appl. Crystallogr. 49 (2016) 2.
[150] A. Tremsin et al., Strain 52 (6) (2016) 548.
[151] W.E. Frazier, J. Mater. Eng. Perform. 23 (6) (2014) 1917.
[152] D. Gu et al., Int. Mater. Rev. 57 (3) (2012) 133.
[153] I. Gibson et al., Additive Manufacturing Technologies, Springer, 2010.
[154] R.R. Dehoff et al., Mater. Sci. Technol. 31 (8) (2015) 931.
[155] H.J. Kirkwood et al., Int. J. Nanotechnol. 14 (1–6) (2017) 166.
[156] A.S. Tremsin et al., Sci. Technol. Adv. Mater. 17 (1) (2016) 324.
[157] H.Z. Bilheux et al., Advances in Neutron Radiography: Application to Additive Manufacturing Inconel 718; 0882-7958, Oak Ridge National Laboratory (ORNL), Oak Ridge, TN (United States), High Temperature Materials Laboratory (HTML); Spallation Neutron Source, 2016.
[158] A.S. Tremsin et al., Sci. Rep. 7 (2017) 40759.
[159] S.W. Lee et al., Appl Phys Express 3 (2010) 106602.

[160] C. Grunzweig et al., Phys. Rev. Lett. 101 (2008) 2.
[161] C. Grunzweig et al., J. Appl. Phys. 107 (2010) 9.
[162] A. Hubert, R. Schäfer, Magnetic Domains, Springer, 1998.
[163] R. Schafer, S. Schinnerling, J. Magn. Magn. Mater. 215 (2000) 140.
[164] T. Reimann et al., J. Appl. Crystallogr. 49 (5) (2016) 1488.
[165] J. Auer, H. Ullmaier, Phys. Rev. B 7 (1) (1973) 136.
[166] M. Dawson et al., New J. Phys. 11 (4) (2009) 043013.
[167] M. Strobl et al., Appl. Phys. Lett. 91 (2007) 25.
[168] M. Strobl et al., Physica B 404 (17) (2009) 2611.
[169] M. Strobl et al., Physica B 406 (12) (2011) 2415.
[170] I. Manke et al., J. Appl. Phys. 104 (7) (2008) 076109.
[171] N. Kardjilov et al., Nucl. Instrum. Methods Phys. Res., Sect. A 605 (1–2) (2009) 13.
[172] A. Hilger, Characterization of Magnetic Structures by Imaging Methods with Cold Neutrons, Technische Universität, Berlin, 2010.
[173] J.M. Warren et al., Plant Soil 366 (1–2) (2013) 683.
[174] C. Tötzke et al., Sci. Rep. 7 (1) (2017) 6192.
[175] U. Matsushima et al., Nucl. Instrum. Methods Phys. Res., Sect. A 605 (1) (2009) 146.
[176] S.E. Oswald et al., Vadose Zone J. 7 (3) (2008) 1035.
[177] A. Carminati et al., Plant Soil 332 (1–2) (2010) 163.
[178] F. Kim et al., J. Comput. Civil Eng. 29 (6) (2014) 04014096.
[179] F.H. Kim et al., J. Geotech. Geoenviron. Eng. 138 (2) (2011) 147.
[180] F.H. Kim et al., J. Geotech. Geoenviron. Eng. 139 (5) (2012) 715.
[181] F.H. Kim, Dual-Modality (Neutron and X-ray) Imaging for Characterization of Partially Saturated Granular Materials and Flow Through Porous Media, University of Tennessee, 2013.
[182] F.H. Kim et al., Int. J. Impact Eng. 89 (2016) 72.
[183] E. Perfect et al., Earth Sci. Rev. 129 (2014) 120.
[184] S.A. Hall, Geophys. Res. Lett. 40 (11) (2013) 2613.
[185] S. Hall et al., Local characterisation of fluid flow in sandstone with localised deformation features through fast neutron imaging, in: EPJ Web of Conferences, EDP Sciences, 2010.
[186] E. Tudisco et al., Physics Procedia 69 (2015) 509.
[187] N. Kardjilov et al., J. Appl. Crystallogr. 49 (2016) 1.
[188] N. Kardjilov et al., J. Large-Scale Res. Facil. 2 (2016) A98.
[189] N. Kardjilov et al., Nucl. Instrum. Methods Phys. Res., Sect. A 651 (1) (2011) 47.
[190] E. Calzada et al., Nucl. Instrum. Methods Phys. Res., Sect. A 605 (1–2) (2009) 50.
[191] F. Salvemini et al., J. Anal. At. Spectrom. 27 (9) (2012) 1494.
[192] K. Kino et al., Physics Procedia 43 (2013) 360.
[193] E. Barzagli et al., Eur. Phys. J. Plus 129 (7) (2014) 158.
[194] Y. Kiyanagi et al., Restaurierung und Archäologie 8 (2015) 85.
[195] A. Fedrigo et al., Archaeol. Anthropol. Sci. (2016) 1.
[196] N. Kardjilov et al., Neutron imaging, in: Neutron Methods for Archaeology and Cultural Heritage, Springer International Publishing, 2017, p. 329.
[197] A. Masalles et al., Physics Procedia 69 (2015) 636.
[198] C. Grünzweig et al., Physics Procedia 43 (2013) 231.
[199] C. Grünzweig et al., MTZ Worldw. 73 (4) (2012) 56.
[200] B. Khaykovich et al., Nucl. Instrum. Methods Phys. Res., Sect. A 631 (1) (2011) 98.
[201] D. Liu et al., Appl. Phys. Lett. 102 (18) (2013) 183508.
[202] D. Liu et al., Nat. Commun. (2013) 4.
[203] P.E. Vanier, Opt. Eng. 2003 (1999) 124.
[204] M. Schulz et al., Nucl. Instrum. Methods Phys. Res., Sect. A 605 (1–2) (2009) 33.
[205] D.S. Hussey et al., Physics Procedia 69 (2015) 48.
[206] R. Woracek et al., Nucl. Instrum. Methods Phys. Res., Sect. A 839 (2016) 102.
[207] W.R. Lionheart, P.J. Withers, Inverse Prob. 31 (4) (2015) 045005.
[208] B. Abbey et al., Procedia Eng. 1 (1) (2009) 185.
[209] B. Abbey et al., Nucl. Instrum. Methods Phys. Res., Sect. B 270 (2012) 28.
[210] B. Abbey et al., Int. J. Mater. Res. 103 (2) (2012) 234.
[211] H.J. Kirkwood et al., Trans. Am. Crystallogr. Assoc. 44 (2013) 182.
[212] W. Li et al., Characterisation of residual stress due to fillet rolling on bolts made of a nickel base superalloy, in: Advanced Materials Research, Vol. 996, Trans Tech Publ, 2014, p. 670.
[213] C. Wensrich et al., Strain 52 (1) (2016) 80.
[214] C. Wensrich et al., Nucl. Instrum. Methods Phys. Res., Sect. B 383 (2016) 52.
[215] K. Doi et al., J. Appl. Crystallogr. 4 (6) (1971) 528.
[216] M. Ando, S. Hosoya, Phys. Rev. Lett. 29 (5) (1972) 281.
[217] M. Schlenker, J. Baruchel, Physica B+ C 137 (1–3) (1986) 309.
[218] J. Baruchel, Neutron News 3 (3) (1992) 20.
[219] N. Kardjilov, Further Developments and Applications of Radiography and Tomography with Thermal and Cold Neutrons PhD Thesis, Universität München, 2003.
[220] M.J. Gutmann et al., J. Appl. Crystallogr. 39 (1) (2006) 82.
[221] S. Peetermans et al., Analyst 139 (22) (2014) 5766.
[222] A. Cereser, Time-of-flight 3D Neutron Diffraction for Multigrain Crystallography, Technical University of Denmark, Denmark, 2016.
[223] Cereser Alberto et al., Sci. Rep. (2017).
[224] A.S. Tremsin et al., IEEE Trans. Nucl. Sci. 59 (6) (2012) 3272.
[225] H. Sato et al., Nucl. Instrum. Methods Phys. Res., Sect. A 605 (1) (2009) 36.
[226] E.P. Cippo et al., J. Anal. At. Spectrom. 26 (5) (2011) 992.
[227] A.S. Tremsin et al., J. Nucl. Mater. 440 (1–3) (2013) 633.
[228] A.S. Tremsin et al., AIP Adv. 7 (1) (2017) 015315.
[229] A.S. Tremsin et al., Sci. Rep. (2017) 7.
[230] A.S. Tremsin et al., J. Appl. Crystallogr. 49 (2016) 4.
[231] A. Hilger et al., J. Appl. Phys. 107 (3) (2010) 036101.
[232] W.G. Bouwman et al., Physica B 350 (1) (2004) E787.
[233] M. Strobl et al., J. Appl. Crystallogr. 49 (2016) 2.
[234] R.P. Harti et al., Sci. Rep. (2017) 7.
[235] M. Strobl et al., J. Appl. Phys. 112 (1) (2012) 014503.
[236] M. Strobl et al., Sci. Rep. 5 (2015) 16576.
[237] M. Sales et al., IOP Conf. Ser.: J. Phys. Conf. Series (2017) 862.
[238] M. Strobl et al., Physica B 407 (21) (2012) 4132.